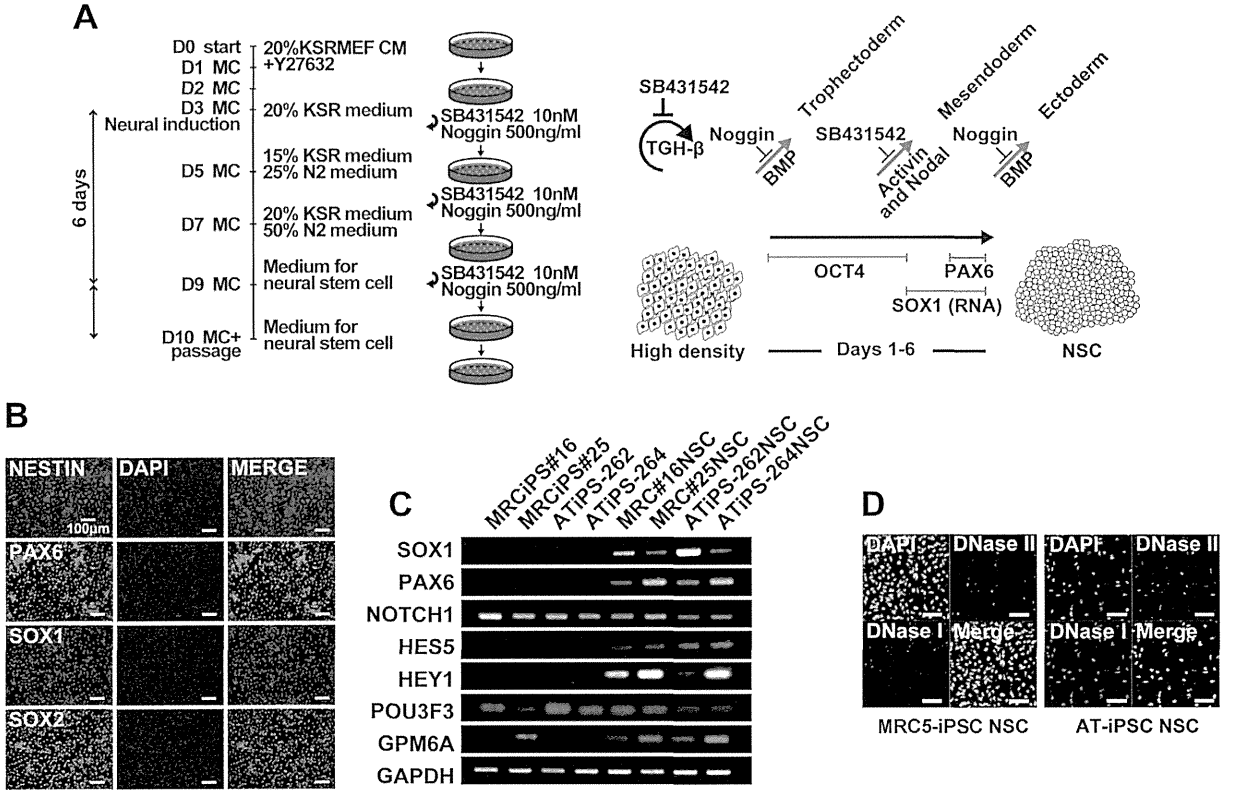

Figure 6 | Neural differentiation of AT-iPS cells. (A).Protocol for neural differentiation of AT-iPS cells. Neural differentiation of iPS cells was performed according to the standard protocol[37]. MC: Medium change. (B). Immunocytochemistry of AT-iPS cells (ATiPS-262). (C). RT-PCR analysis on AT-iPS cells (ATiPS-262, ATiPS-264) and MRC5-iPS cells (MRCiPS#16, MRCiPS#25) after neural differentiation. Primers are listed in Supplemental Table S1. (D). Apoptosis of AT-iPS cells after neural differentiation. Apoptosis was detected by the ApopTag ISOL Dual Fluorescence Apoptosis Detection Kit (DNase Types I & II) APT1000 (Millipore). Left panels: neural differentiation of MRC5-iPS cells (MRCiPS#25), right panels: neural differentiation of AT-iPS cells (ATiPS-262).

(Supplemental Figure S7B, C). These results indicate that AT-iPS cells have higher radiation sensitivity than the intact iPS cells when growth characteristics are considered.

Karyotypic analyses of AT-iPS cells and MRC5-iPS cells were performed after X-ray irradiation, and did not reveal any significant difference in the radiation sensitivity. Most cells analyzed showed an intact chromosomal pattern even after longer cultivation (ATiPS-264: Passage 81 and 20 months, ATiPS-024: Passage 86 and 22 months). Only low frequencies of chromosomal abnormalities such as chromosomal loss and amplification, deletion, and translocation were detected in AT-iPS cells; MRC5-iPS cells showed similar results (Figure 5D).

Neural differentiation of iPS cells. Since one of the most common symptoms in patients with ataxia telangiectasia is neural impairment, we investigated neural differentiation of AT-iPS cells (ATiPS-262 and -264) and MRC5-iPS cells (MRCiPS#16 and #25) (Figure 6A). AT-iPS cells exhibited neural phenotypes by morphological analysis, immunocytochemistry (Figure 6B), and RT-PCR analysis (Figure 6C, Supplemental Figure S8), and no significant difference between AT-iPS cells and MRC5-iPS cells were detected. However, apoptosis significantly increased after neural differentiation of AT-iPS cells, compared with MRC5-iPS cells (Figure 6D). We obtained consistent results from all iPS cells examined.

Discussion

Human pluripotent stem cells deficient for the ATM gene have successfully been generated in two ways: Disruption of the ATM gene in human ES cells by genetic manipulation with bacterial artificial chromosome and derivation of disease-specific iPS cells from patients with ataxia telangiectasia[11–13]. The ATM-deficient pluripotent stem cells serve as disease model cells for clarification of pathogenic mechanisms and for screening novel compounds to treat the disease. In this study, we generated iPS cells from fibroblasts (AT1OS) of a human AT patient, and compared them with those from a healthy donor. The AT-iPS cells exhibited the same proliferation activity as wild type-iPS cells (WT-iPS cells), a gene expression profile characteristic of pluripotent stem cells such as ES cells and WT-iPS cells, the capability to differentiate into all three germ layers, and hypersensitivity in growth characteristics to X-ray irradiation. Apoptosis could be induced upon neural differentiation of AT-iPS cells. These results indicate that the established cells kept both characteristics of pluripotent stem cells and *ATM*-deficient cells.

Though normal ATM function was not a prerequisite for the establishment and maintenance of iPS cells, the reprogramming efficiency of the fibroblasts derived from an AT patient was extremely low, suggesting indirect roles of ATM in the somatic reprogramming process. One of the major targets of ATM is p53[14], and ATM-dependent phosphorylation is directly responsible for p53 activation. ATM and p53 are two proteins that are believed to play a major role in maintaining the integrity of the genome. In spite of having the related function of maintaining the integrity of the genome, p53 is known to serve as a barrier in iPS cell generation. Genetic ablation or decreased amounts of p53 remarkably increases reprogramming efficiency in mouse and human somatic cells[15–19]. Thus, ATM and p53

appear to have opposite roles on the reprogramming of differentiated cells to pluripotent cells. ATM kinase phosphorylates a broad range of substrates, and is involved in a wider range of safeguard systems than p53, such as DNA repair, apoptosis, G1/S, intra-S checkpoint and G2/M checkpoints. Thus, p53-independent reprogramming processes may have a crucial need for some ATM functions, and other phosphatidyl-inositol 3-kinase like enzymes, such as ATR, may partially compensate the ATM-deficiency.

Alternatively, telomere damage may explain the low reprogramming efficiency found in AT-derived fibroblasts. Telomeres found at the ends of eukaryotic chromosomes prevent their erosion, facilitate the recruitment of telomere-binding factors and stop the activation of the DNA damage response pathways. In humans, *ATM* deficiency results in accelerated telomere loss, and T lymphocytes derived from AT-patients exhibit frequent telomeric fusions[20]. Mouse cells with short telomeres cannot be reprogrammed to iPS cells despite their normal proliferation rates, probably reflecting the existence of 'reprogramming barriers' that abort the reprogramming of cells with uncapped telomeres[21,22].

Unexpectedly, we found that AT-iPS cells did not show any chromosomal instability *in vitro*, i.e., maintenance of intact chromosomes was observed after 80 passages (560 days). Even after X-ray irradiation at low dose, the most of AT-iPS cells still maintained an intact karyotype. In contrast, the parental fibroblastic cell line, AT1OS, showed frequent chromosomal abnormalities, such as deletion, addition and translocation. However, the AT-iPS cells still exhibited hypersensitivity to X-ray irradiation in the growth profile, which are major characteristics of ATM-deficient cells. These results indicate that AT-iPS cells maintain the defective response to ionizing irradiation, but that the defects do not affect maintenance of intact chromosomes.

What are the causes of the differences in the chromosomal stability between AT-iPS cells and AT1OS cells, the source of AT-iPS cells? The major difference between iPS cells and somatic cells may be the ability to undergo unlimited self-renewal. Somatic cells usually have limited growth potential, gradually decline with advancing age, and finally fall into senescence. In contrast, pluripotent stem cells are characterized by unlimited self-renewal and the ability to generate differentiated functional cell types. One of the causes of immortality is the presence of a terminal DNA polymerase capable of synthesizing telomeres, and somatic cell mortality is the result of a progressive loss of the telomeric DNA because of the absence of the immortalizing polymerase. The function of telomerase in terminal DNA elongation is necessary in order to overcome the "end-replication problem" whereby conventional DNA polymerases cannot fully replicate linear DNAs[23]. Telomere erosion (by 50–100 bp per cellular division) limits the replicative capacity of the majority of somatic cells, which do not express active telomerase[24]. In humans, *ATM* deficiency results in accelerated telomere loss in somatic cells, and T lymphocytes derived from AT patients exhibit frequent chromosomal instability[20].

Response to oxidative stress may be one of the causes of the accelerated telomere loss. It has been suggested that somatic cells, such as fibroblasts and neuronal cells from AT patients are in a chronic state of oxidative stress, which could contribute to their enhanced telomere shortening[25]. ATM protein is suggested to have a role in the prevention or repair of oxidative damage to telomeric DNA, and enhanced sensitivity of telomeric DNA to oxidative damage in AT cells results in accelerated telomere shortening and chromosomal instability. Further study using telomerase inhibitors and anti-oxidants using the human AT-iPS cells may clarify the cause of the difference between somatic cells and iPS cells derived from AT patients.

The number of single-nucleotide mutations per cell genome was estimated from 22 human iPS cells by extensive exome analysis on protein-coding sequences[26]. The exome analysis on the AT-iPS cell lines from 17 to 27 passages after the establishment in this study included not only coding but also untranslated, non-coding RNA, and their adjacent regions, covering up to 93.9 Mb. The number of observed coding mutations during reprogramming was comparable or smaller in all the three lines than those reported by the preceding study[26], supporting a genetic stability of the AT-iPS cells.

AT is characterized by early onset progressive cerebellar ataxia, oculocutaneous telangiectasia, susceptibility to bronchopulmonary disease, and lymphoid tumors. The pathologic tissues are generally not easily accessible, resulting in a substantial disadvantage for medical and biological studies of the pathogenesis of the disease and for development of novel therapeutic interventions. Generation of *Atm*-deficient mice partially overcomes such difficulties. However, oculocutaneous telangiectasias and histological evidence of neuronal degeneration, which are characteristics of human AT patients, have not seen in these mice, suggesting that the mouse model for AT is limited. Thus, the established human AT-iPS cells described in this study show promise as a tool for clarifying the pathogenesis of AT, and may facilitate development of drugs that inhibit ataxia and hypersensitivity to ionizing radiation.

Methods

Ethical statement. Human cells in this study were performed in full compliance with the Ethical Guidelines for Clinical Studies (2008 Notification number 415 of the Ministry of Health, Labor, and Welfare). The cells were banked after approval of the Institutional Review Board at the National Institute of Biomedical Innovation (May 9, 2006).

Human cells. AT1OS cells were obtained from a ten-year-old Japanese boy (JCRB Cell Bank, Osaka, Japan). The patient history is contained in the original report[27]. The patient was referred to the hospital because of progressive cerebellar ataxia and repeated upper respiratory infection. He raised his head well at 5 months and walked alone at 14 months of age. At the age of 2 years, his parents first noticed his tottering gait. He suffered from severe suppurative tympanitis at 4 years of age, since then he was recurrently afflicted with upper respiratory infections. Before school age, he had already developed a progressive ataxic gait. At the age of 10 years, he could walk alone only a short distance. The neurological examination revealed hyporeflexia, choreoathetosis, oculomotor apraxia and cerebellar dysarthria. Telangiectasia was seen in his bulbar conjunctivae. He showed mild mental retardation (IQ, 72). X-ray computed tomography revealed the fourth ventricular enlargement, suggesting mild cerebellar atrophy. Laboratory tests disclosed a decreased serum level of IgA (17 mg/dl) and a markedly elevated level of α-fetoprotein (560 ng/ml). Serum IgE and IgM were within normal levels. His parents are first cousins.

AT1OS cells were cultured in culture dishes (100 mm, Becton Dickinson). All cultures were maintained at 37°C in a humidified atmosphere containing 95% air and 5% CO_2. When the cultures reached subconfluence, the cells were harvested with a Trypsin-EDTA solution (cat# 23315, IBL CO., Ltd, Gunma, Japan), and re-plated at a density of 5×10^5 cells in a 100-mm dish. Medium changes were carried out twice a week thereafter. MRC5-iPS cells were maintained on irradiated MEFs as previously described[28,29]. MRC5iPS#16 (Fetch), MRC5iPS#25 (Tic), and MRC5iPS#40 (Skipper) were used as controls for AT-iPS cells. MRC5 (ATCC, CCL-171), a parental cell of MRC5-iPS cells, is from lung fibroblasts of 14-week fetus (Caucasian male).

Generation of iPS cells. AT-iPS cells were generated according to the method as previously described[28]. Briefly, to produce VSV-G (vesicular stomatitis virus G glycoprotein) retroviruses, 293FT cells (Invitrogen) were plated at 2×10^6 cells per 10-cm culture dish with DMEM supplemented with 10% FBS, and incubated overnight. On the next day, the cells were co-transfected with pMXs-OCT4, SOX2, KLF4 or c-MYC, pCL-GagPol, and pHCMV-VSV-G vectors using the TransIT-293 reagent (Mirus Bio LLC, Madison WI). The virus-containing supernatants were collected 48 h after incubation. The supernatants were filtered through a 0.45 μm pore-size filter, centrifuged, and then resuspended in DMEM supplemented with 4 μg/ml polybrene (Nacalai Tesque, Kyoto, Japan). Human AT1OS cells were seeded at 1.0×10^5 cells per well of 6-well plate 24 h before infection. A 1 : 1 : 1 : 1 mixture of OCT3/4, SOX2, KLF4, and c-MYC viruses was added to AT1OS cells[28–31]. The retrovirus carrying the EGFP gene was infected to estimate infection efficiency in a separate experiment. One-half of the medium was changed every day and colonies were picked up at around day 28.

RT-PCR. Total RNA was isolated from cells using the TRIzol (Invitrogen) or the RNeasy Plus Mini Kit (Qiagen). cDNA was synthesized from 1 μg of total RNA using Superscript III reverse transcriptase (Invitrogen) with random hexamers according to the manufacturer's instructions. Template cDNA was PCR-amplified with gene-specific primer sets (Supplemental Table S1).

Quantitative RT-PCR. RNA was extracted from cells using the RNeasy Plus Mini kit (Qiagen). An aliquot of total RNA was reverse transcribed using an oligo (dT) primer. For the thermal cycle reactions, the cDNA template was amplified (ABI PRISM

7900HT Sequence Detection System) with gene-specific primer sets using the Platinum Quantitative PCR SuperMix-UDG with ROX (11743-100, Invitrogen) under the following reaction conditions: 40 cycles of PCR (95°C for 15 s and 60°C for 1 min) after an initial denaturation (95°C for 2 min). Fluorescence was monitored during every PCR cycle at the annealing step. The authenticity and size of the PCR products were confirmed using a melting curve analysis (using software provided by Applied Biosystems) and a gel analysis. mRNA levels were normalized using GAPDH as a housekeeping gene.

Western blot analysis. Western blot analysis of total cell lysate for p53 and phospho-p53(Ser15) and of nuclear fractions for ATM was performed as described[32]. The membrane filter was probed with the antibodies to p53 (Enzo Life Sci., BML-SA293), phosphor-p53 (S15) (Cell signaling, #9284), and ATM (MBL, PM026), and then incubated with HRP-conjugated antibody to rabbit IgG. The protein signals were detected by ECL detection (Amersham).

Immunocytochemical analysis. Cells were fixed with 4% paraformaldehyde in PBS for 10 min at 4°C. After washing with PBS and treatment with 0.2% trypsin in PBS (PBST) for 10 min at 4°C, cells were pre-incubated with blocking buffer (10% goat serum in PBS) for 30 min at room temperature, and then reacted with primary antibodies in blocking buffer for 12 h at 4°C. Followed by washing with 0.2% PBST, cells were incubated with secondary antibodies; anti-rabbit or anti-mouse IgG conjugated with Alexa 488 or 546 (1 : 300) (Invitrogen) in blocking buffer for 1 h at room temperature. Then, the cells were counterstained with DAPI and mounted.

Karyotypic analysis. Karyotypic analysis was contracted out at Nihon Gene Reserch Laboratories Inc. (Sendai, Japan). Metaphase spreads were prepared from cells treated with 100 ng/mL of Colcemid (Karyo Max, Gibco Co. BRL) for 6 h. The cells were fixed with methanol : glacial acetic acid (2 : 5) three times, and dropped onto glass slides (Nihon Gene Reserch Laboratories Inc.). Chromosome spreads were Giemsa banded and photographed. A minimum of 10 metaphase spreads were analyzed for each sample, and karyotyped using a chromosome imaging analyzer system (Applied Spectral Imaging, Carlsbad, CA).

Quantitative fluorescence in situ hybridization (Q-FISH). We measured telomere length by Q-FISH analysis as previously described[33–35]. The parental cells and iPS cells were subjected to telomere measurements by the telomere fluorescent intensities of the p- and q-arms of all the chromosomes in the metaphase spread individually. The telomere lengths were determined by the median telomere fluorescent unit values.

Exome sequencing. Approximately 2.0 μg of genomic DNA from each cell sample was sonicated to give a fragment size of 200 bp on a Covaris S220 instrument. After 5–6 cycles of PCR amplification, capture and library preparation were performed with Agilent SureSelect Human All Exon V4 + UTRs + lincRNA (80 Mb), followed by washing, elution, and additional 10-cycle PCR. Enriched libraries were sequenced on an Illumina HiSeq 1000 operated in 101-bp paired-end mode. Image analyses and base calling on all lanes of data were performed using CASAVA 1.8.2 with default parameters.

Read mapping and variant analysis. Reads from each sample were first trimmed by removing adapters and low quality bases at ends using Trimmomatic 0.22 and then aligned to the hs37d5 sequence (hg19 and decoy sequences) using the Burrows-Wheeler Aligner 0.6.2. Uniquely mapped reads were selected by a custom script, converted from sam to bam using SAMtools 0.1.18, and processed by Picard 1.83 to mark PCR duplicates. Genome Analysis Toolkit (GATK) 2.3–9 was then used to remove the duplicates, perform local realignment and map quality score recalibration to produce calibrated bam files for each sample. Multi-sample callings for SNVs were made by GATK. Target regions for variant detection were expanded to 93.9 Mb in total by following the manufacturer's instruction. The annotated VCF files were then filtered using GATK with a stringent filter setting and custom scripts. Variant calls which failed to pass the following filters were eliminated: QUAL < 400 || QD < 2.0 || MQ < 40.0 || FS > 60.0 || HaplotypeScore > 13.0 || GQ <= 60. When genotype is 0/1, 0/2, or 1/2, only SNVs that meet the following conditions were selected: both of the allelic depths >= 8 && difference of the allelic depths within twofold. When genotype is 0/0, 1/1, or 2/2, only SNVs that meet the following conditions were selected: difference of the allelic depths no less than 32-fold, one allelic depth is 1 and the other is no less than 16, or one allelic depth is 0 and the other is no less than 8. Annotations of altered bases were made using SnpEff 3.1 based on GRCh37.69[36]. Custom Perl scripts and C programs are available at http://github.com/glires/genomics/.

Structural mutation analysis. The structural mutation analysis by genome-wide SNP genotyping was performed using Illumina HumanCytoSNP-12 v2.1 DNA Analysis BeadChip Kit. The microarray contains approximately 300,000 SNP markers with an average call frequency of > 99%. Subsequent computational and manual analyses were performed using the Illumina KaryoStudio software. The data have been submitted to the GEO database under accession number GSE54576.

Irradiation. Cells were irradiated by X-ray at 0.87 Gy/min, using MBR-1520R-3 (Hitachi, Tokyo, Japan). Immediately after irradiation, cells were returned to the incubator at 37°C in a humidified atmosphere containing 95% air and 5% CO_2, and incubated until further processing. Cell number was counted with Vi-CELL 1.00. (Beckman Coulter K.K.,Tokyo, Japan).

Teratoma formation. AT-iPS cells were harvested by accutase treatment, collected into tubes, and centrifuged. The same volume of Basement Membrane Matrix (354234, BD Biosciences) was added to the cell suspension. The cells ($>1 \times 10^7$) were subcutaneously inoculated into immuno-deficient, non-obese diabetic (NOD)/severe combined immunodeficiency (SCID) mice (CREA, Tokyo, Japan). After 6 to 10 weeks, the resulting tumors were dissected and fixed with PBS containing 4% paraformaldehyde. Paraffin-embedded tissue was sliced and stained with hematoxylin and eosin (HE). The operation protocols were accepted by the Laboratory Animal Care and the Use Committee of the National Research Institute for Child and Health Development, Tokyo.

Neural differentiation of iPS cells. We employed the standard protocol for neural differentiation of iPS cells[37,38]. Apoptosis was detected by the ApopTag ISOL Dual Fluorescence Apoptosis Detection Kit (DNase Types I & II) APT1000 (Millipore), according to the manufacturer's protocol.

1. Takahashi, K. & Yamanaka, S. Induction of pluripotent stem cells from mouse embryonic and adult fibroblast cultures by defined factors. *Cell* **126**, 663–676 (2006).
2. Yu, J. *et al.* Induced pluripotent stem cell lines derived from human somatic cells. *Science* **318**, 1917–1920 (2007).
3. Hankowski, K. E., Hamazaki, T., Umezawa, A. & Terada, N. Induced pluripotent stem cells as a next-generation biomedical interface. *Lab Invest* **91**, 972–977 (2011).
4. Mavrou, A., Tsangaris, G. T., Roma, E. & Kolialexi, A. The ATM gene and ataxia telangiectasia. *Anticancer Res* **28**, 401–405 (2008).
5. McKinnon, P. J. ATM and ataxia telangiectasia. *EMBO reports* **5**, 772–776 (2004).
6. Kurz, E. U. & Lees-Miller, S. P. DNA damage-induced activation of ATM and ATM-dependent signaling pathways. *DNA Repair (Amst)* **3**, 889–900 (2004).
7. Gatei, M. *et al.* Role for ATM in DNA damage-induced phosphorylation of BRCA1. *Cancer Res* **60**, 3299–3304 (2000).
8. Barlow, C. *et al.* Atm-deficient mice: a paradigm of ataxia telangiectasia. *Cell* **86**, 159–171 (1996).
9. Kinoshita, T. *et al.* Ataxia-telangiectasia mutated (ATM) deficiency decreases reprogramming efficiency and leads to genomic instability in iPS cells. *Biochem Biophys Res Commun* **407**, 321–326 (2011).
10. Kuljis, R. O., Xu, Y., Aguila, M. C. & Baltimore, D. Degeneration of neurons, synapses, and neuropil and glial activation in a murine Atm knockout model of ataxia-telangiectasia. *Proc Natl Acad Sci U S A* **94**, 12688–12693 (1997).
11. Song, H., Chung, S. K. & Xu, Y. Modeling disease in human ESCs using an efficient BAC-based homologous recombination system. *Cell Stem Cell* **6**, 80–89 (2010).
12. Lee, P. *et al.* SMRT compounds abrogate cellular phenotypes of ataxia telangiectasia in neural derivatives of patient-specific hiPSCs. *Nat Commun* **4**, 1824 (2013).
13. Nayler, S. *et al.* Induced pluripotent stem cells from ataxia-telangiectasia recapitulate the cellular phenotype. *Stem Cells Transl Med* **1**, 523–535 (2012).
14. Meek, D. W. The p53 response to DNA damage. *DNA Repair (Amst)* **3**, 1049–1056 (2004).
15. Hong, H. *et al.* Suppression of induced pluripotent stem cell generation by the p53-p21 pathway. *Nature* **460**, 1132–1135 (2009).
16. Kawamura, T. *et al.* Linking the p53 tumour suppressor pathway to somatic cell reprogramming. *Nature* **460**, 1140–1144 (2009).
17. Li, H. *et al.* The Ink4/Arf locus is a barrier for iPS cell reprogramming. *Nature* **460**, 1136–1139 (2009).
18. Marion, R. M. *et al.* A p53-mediated DNA damage response limits reprogramming to ensure iPS cell genomic integrity. *Nature* **460**, 1149–1153 (2009).
19. Utikal, J. *et al.* Immortalization eliminates a roadblock during cellular reprogramming into iPS cells. *Nature* **460**, 1145–1148 (2009).
20. Metcalfe, J. A. *et al.* Accelerated telomere shortening in ataxia telangiectasia. *Nat Genet* **13**, 350–353 (1996).
21. Marion, R. M. *et al.* Telomeres acquire embryonic stem cell characteristics in induced pluripotent stem cells. *Cell Stem Cell* **4**, 141–154 (2009).
22. Davy, P. & Allsopp, R. Balancing out the ends during iPSC nuclear reprogramming. *Cell Stem Cell* **4**, 95–96 (2009).
23. Watson, J. D. Origin of concatemeric T7 DNA. *Nat New Biol* **239**, 197–201 (1972).
24. Harley, C. B., Futcher, A. B. & Greider, C. W. Telomeres shorten during ageing of human fibroblasts. *Nature* **345**, 458–460 (1990).
25. Tchirkov, A. & Lansdorp, P. M. Role of oxidative stress in telomere shortening in cultured fibroblasts from normal individuals and patients with ataxia-telangiectasia. *Hum Mol Genet* **12**, 227–232 (2003).
26. Gore, A. *et al.* Somatic coding mutations in human induced pluripotent stem cells. *Nature* **471**, 63–67 (2011).
27. Ikenaga, M., Midorikawa, M., Abe, J. & Mimaki, T. The sensitivities to radiations and radiomimetic chemicals of cells from patients with ataxia telangiectasia. *Jinrui Idengaku Zasshi* **28**, 1–10 (1983).

28. Makino, H. *et al.* Mesenchymal to embryonic incomplete transition of human cells by chimeric OCT4/3 (POU5F1) with physiological co-activator EWS. *Exp Cell Res* **315**, 2727–2740 (2009).
29. Nishino, K. *et al.* DNA Methylation Dynamics in Human Induced Pluripotent Stem Cells over Time. *PLoS Genet* **7**, e1002085 (2011).
30. Nagata, S. *et al.* Efficient reprogramming of human and mouse primary extra-embryonic cells to pluripotent stem cells. *Genes Cells* **14**, 1395–1404 (2009).
31. Nishino, K. *et al.* Defining hypo-methylated regions of stem cell-specific promoters in human iPS cells derived from extra-embryonic amnions and lung fibroblasts. *PLoS One* **5**, e13017 (2010).
32. Toyoda, M., Kojima, M. & Takeuchi, T. Jumonji is a nuclear protein that participates in the negative regulation of cell growth. *Biochem Biophys Res Commun* **274**, 332–336 (2000).
33. Poon, S. S. & Lansdorp, P. M. Measurements of telomere length on individual chromosomes by image cytometry. *Methods Cell Biol* **64**, 69–96 (2001).
34. Terai, M. *et al.* Investigation of telomere length dynamics in induced pluripotent stem cells using quantitative fluorescence *in situ* hybridization. *Tissue Cell* **45**, 407–413 (2013).
35. Takubo, K. *et al.* Chromosomal instability and telomere lengths of each chromosomal arm measured by Q-FISH in human fibroblast strains prior to replicative senescence. *Mech Ageing Dev* **131**, 614–624 (2010).
36. Cingolani, P. *et al.* A program for annotating and predicting the effects of single nucleotide polymorphisms, SnpEff: SNPs in the genome of Drosophila melanogaster strain w1118; iso-2; iso-3. *Fly (Austin)* **6**, 80–92 (2012).
37. Chambers, S. M. *et al.* Highly efficient neural conversion of human ES and iPS cells by dual inhibition of SMAD signaling. *Nat Biotechnol* **27**, 275–280 (2009).
38. Koch, P., Opitz, T., Steinbeck, J. A., Ladewig, J. & Brüstle, O. A rosette-type, self-renewing human ES cell-derived neural stem cell with potential for in vitro instruction and synaptic integration. *Proc Natl Acad Sci U S A* **106**, 3225–3230 (2009).

Acknowledgments

We would like to express our sincere thanks to M. Yamada for fruitful discussion and critical reading of the manuscript, to H. Abe and H. Kobayashi for providing expert technical assistance, to Dr. C. Ketcham for English editing and proofreading, and to E. Suzuki, Y. Kajiyama, Y. Suehiro, and K. Saito for secretarial work. This research was supported by grants from the Ministry of Education, Culture, Sports, Science, and Technology (MEXT) of Japan; by Ministry of Health, Labor and Welfare (MHLW) Sciences research grants; by a Research Grant on Health Science focusing on Drug Innovation from the Japan Health Science Foundation; by the program for the promotion of Fundamental Studies in Health Science of the Pharmaceuticals and Medical Devices Agency; by the Grant of National Center for Child Health and Development. We acknowledge the International High Cited Research Group (IHCRG #14-104), Deanship of Scientific Research, King Saudi University, Riyadh, Kingdom of Saudi Arabia. AU thanks King Saud University, Riyadh, Kingdom of Saudi Arabia, for the Visiting Professorship.

Author contributions

A.U. designed experiments. Y.F., M.T., K.O., K.Nakamura, K.Nakabayashi, M.Y.I. and K.T. performed experiments. Y.F., M.T., K.O., K.Nakabayashi, M.Y.I., M.N., K.Hata and K.Hanaoka analyzed data. Y.F., M.T., K.O., K.Nakabayashi, S.T., M.Y.I., M.N., K.Hata, AH, and K.Hanaoka contributed reagents, materials and analysis tools. A.M. and A.U. wrote this manuscript.

Additional information

Accession codes The SNP genotyping by SNP array data was uploaded to the ncbi web site (GSE47498: Increased X-ray sensitivity and sustained chromosomal stability in Ataxia Telangiectasia-derived induced pluripotent stem (AT-iPS) cells, GSM1151202: AT1OS cells, GSM1151203: ATiPS-262 cells at passage 17, GSM1151204: ATiPS-263 cells at passage 27, GSM1151205: ATiPS-264 cells at passage 25, GSM1151206: ATiPS-024 cells at passage 25). The exome data was uploaded to the DDBJ Sequence Read Archive (DRP001084).

Supplementary information accompanies this paper at http://www.nature.com/scientificreports

Competing financial interests: The authors declare no competing financial interests.

How to cite this article: Fukawatase, Y. *et al.* Ataxia telangiectasia derived iPS cells show preserved x-ray sensitivity and decreased chromosomal instability. *Sci. Rep.* **4**, 5421; DOI:10.1038/srep05421 (2014).

This work is licensed under a Creative Commons Attribution 4.0 International License. The images or other third party material in this article are included in the article's Creative Commons license, unless indicated otherwise in the credit line; if the material is not included under the Creative Commons license, users will need to obtain permission from the license holder in order to reproduce the material. To view a copy of this license, visit http://creativecommons.org/licenses/by/4.0/

Analysis of somatic hypermutations in the IgM switch region in human B cells

Katsuyuki Horiuchi, MD, PhD,[a] Kohsuke Imai, MD, PhD,[a,b] Kanako Mitsui-Sekinaka, MD,[a] Tzu-Wen Yeh, BSc,[b] Hans D. Ochs, MD, PhD,[c] Anne Durandy, MD, PhD,[d,e,f] and Shigeaki Nonoyama, MD, PhD[a] *Saitama and Tokyo, Japan, Seattle, Wash, and Paris, France*

Background: The molecular mechanism of class-switch recombination (CSR) in human subjects has not been fully elucidated. The CSR-induced mutations occurring in the switch region of the IgM gene (Smu-SHMs) in *in vitro* CSR-activated and *in vivo* switched B cells have been analyzed in mice but not in human subjects.
Objective: We sought to better characterize the molecular mechanism of CSR in human subjects.
Methods: Smu-SHMs were analyzed *in vitro* and *in vivo* by using healthy control subjects and patients with molecularly defined CSR defects.
Results: We found that Smu-SHMs can be induced *in vitro* by means of CSR activation in human subjects. We also found large amounts of Smu-SHMs in *in vivo* class-switched memory B cells, smaller (although significant) amounts in unswitched memory B cells, and very low amounts in naive B cells. In class-switched memory B cells a high frequency of Smu-SHMs was found throughout the Smu. In unswitched memory B cells, the Smu-SHM frequency was significantly decreased in the 5′ part of the Smu. The difference between switched and unswitched B cells suggests that the extension of somatic hypermutation (SHM) to the 5′ upstream region of the Smu might be associated with the effective induction of CSR. The analysis of the pattern of mutations within and outside the WRCY/RGYW (W, A/T; R, A/G; and Y, C/T) motifs, as well as the Smu-SHMs, in CD27$^+$ B cells from CD40 ligand (CD40L)–, activation-induced cytidine deaminase (AID)–, and uracil-DNA glycosylase (UNG)–deficient patients revealed the dependence of Smu-SHM on CD40L, AID, UNG, and the mismatch repair system in human subjects.
Conclusion: CD40L-, AID-, UNG-, and mismatch repair system–dependent Smu-SHMs and extension to the 5′ region of Smu are necessary to accomplish effective CSR in human subjects. (J Allergy Clin Immunol 2014;134:411-9.)

Key words: Activation-induced cytidine deaminase, somatic hypermutation, antibody maturation, uracil-DNA glycosylase, class-switch recombination, immunoglobulin switch region

Several single gene defects are known to cause immunoglobulin class-switch recombination (CSR) defects, resulting in hyper-IgM syndromes. The affected patients have severely impaired IgG, IgA, and IgE production but normal-to-high serum IgM levels associated with recurrent bacterial infections. Of these, 2 gene defects, namely CD40 ligand (CD40L) deficiency and CD40 deficiency, are associated with bacterial and opportunistic infections and unfavorable prognosis. In contrast, patients with B cell–intrinsic CSR defects, including activation-induced cytidine deaminase (AID) deficiency[1] and uracil-DNA glycosylase (UNG) deficiency,[2] have a milder clinical course, particularly when treated with prophylactic immunoglobulin infusions, but frequently have autoimmune diseases.[3]

CSR is the mechanism that induces functional diversity into immunoglobulin molecules. The first step of CSR is the germline transcription of and R-loop formation in the immunoglobulin switch (S) region. In the second step DNA lesions and single-strand DNA breaks are introduced. In the third step the single-strand DNA break leads to double-strand DNA breaks through mechanisms that are not yet fully understood. In the fourth step double-strand DNA breaks are joined by nonhomologous end-joining enzymes, most likely through alternative end-joining using microhomology[4] and not homologous recombination.[5]

In the second step uracil is introduced through the deoxycytidine deamination induced by AID and is then removed by base excision repair molecules to form single-strand DNA breaks. This process requires uracil DNA glycosylase (UNG) and AP-endonuclease, as well as several mismatch repair (MMR) proteins, including PMS2, MSH2, MSH6, and EXO1.[5] During this process, a somatic hypermutation (SHM) is introduced into the S region (S-SHM).[6,7] This S-SHM is likely to be closely associated with CSR but has not been well investigated, particularly in human B cells.

An SHM is also introduced into the variable (V) region of the immunoglobulin gene (V-SHM), which results in production of high-affinity immunoglobulin.[8] Several molecules are known to be used by both V-SHM and S-SHM, but the molecular mechanisms are different and need to be clarified. In AID-deficient

From [a]the Department of Pediatrics, National Defense Medical College, Saitama; [b]the Department of Pediatrics, Tokyo Medical and Dental University (TMDU); [c]the Department of Pediatrics, University of Washington, Seattle; [d]Unité 768, Institut National de la Santé et de la Recherche Médicale (INSERM), Université Paris V René-Descartes, Paris; [e]Service d'Immunologie et d'Hématologie Pédiatrique, Hôpital Necker-Enfants Malades, Assistance Publique-Hôpitaux de Paris; and [f]Institut Federatif de Recherche 94, Site Necker, Faculté de Médecine René Descartes, Université Paris-Descartes, Paris.

Supported in part by grants from the Japan Ministry of Defense; the Japan Ministry of Health, Labour, and Welfare; the Japan Intractable Diseases Research Foundation; the Kawano Masanori Foundation for Promotion of Pediatrics; the Mitsubishi Pharma Research Foundation; l'Institut National de la Santé et de la Recherche Médicale; l'Association de la Recherche Contre le Cancer; the European Union FP7 EUROPAD contract 201549 (EUROPAD); the Agence Nationale pour la Recherche (SVSE3); the National Institutes of Health (R01HD17427-33), the Jeffrey Modell Foundation; and the Immunodeficiency Foundation.

Disclosure of potential conflict of interest: H. D. Ochs is a board member for Sigma Tau and has received support from CSL Behring (committee travel expenses). The rest of the authors declare that they have no relevant conflicts of interest.

Received for publication June 14, 2013; revised February 6, 2014; accepted for publication February 6, 2014.

Available online May 15, 2014.

Corresponding author: Kohsuke Imai, MD, PhD, Department of Community Pediatrics, Perinatal and Maternal Medicine, Tokyo Medical and Dental University (TMDU), 1-5-45, Yushima, Bunkyo-ku, Tokyo 113-8519, Japan. E-mail: kimai.ped@tmd.ac.jp.

0091-6749/$36.00

© 2014 American Academy of Allergy, Asthma & Immunology

http://dx.doi.org/10.1016/j.jaci.2014.02.043

Abbreviations used
AID: Activation-induced cytidine deaminase
CD40L: CD40 ligand
CSR: Class-switch recombination
MMR: Mismatch repair
SHM: Somatic hypermutation
Smu: Switch region of IgM
UNG: Uracil-DNA glycosylase

human subjects and mice, the frequency of V-SHM is extremely decreased.[1,9] In UNG deficiency the frequency of V-SHM is normal, but the introduced DNA sequences are severely skewed.[2] However, although data on S-SHM in dominant-negative AID and UNG-deficient human B cells have been reported,[10] no data are available on purified B-cell populations. After CSR activation in mice, an SHM has also been found in the S region not only near the recombination site but also in the far upstream 5′ region of the highly repetitive S-core region. S-SHMs are induced *in vitro* on CSR activation in Smu regions, as well as in Sgamma, Salpha, and Sepsilon regions, in mice.[6,7,11]

In this study we analyzed SHMs in the Smu region (Smu-SHM, Fig 1) in purified human B cells. We found that an Smu-SHM can be induced by CD40 and IL-4 stimulation, which vigorously induces CSR *in vitro*. The Smu-SHM frequency was different depending on the B-cell maturation stage and was defective in cases of CD40L, AID, and UNG deficiency. The analysis of the mutation pattern of the nucleotides suggests the involvement of a MMR in CSR.

METHODS

Patients and control subjects

Peripheral blood samples were obtained from 4 healthy adults between 32 and 36 years of age (C1-C4) and 3 age-matched healthy children (1, 8, and 11 years old [C5-C7]). P1 was a patient with newly diagnosed AID deficiency (homozygous nonsense mutation leading to W80X) with typical hyper-IgM syndrome (IgM, 386 mg/dL; IgA, <6 mg/dL; and IgG, <10 mg/dL). The other 4 AID-deficient patients (P2-P5) and the 2 UNG-deficient patients (P6 and P7) have been previously reported: P2 and P3 were P5 and P4, respectively, in the study conducted by Revy et al[1]; P4 was the younger brother of P10 and P5 was P12 in the study conducted by Zhu et al[12]; and P6 and P7 were P2 and P3 in the study conducted by Imai et al.[2] P8 to P11 were CD40L-deficient patients. The study was approved by the Institutional Review Board of the National Defense Medical College. Informed consent from each participant or their parents was obtained in accordance with the Declaration of Helsinki.

Detection of SHM in the Smu region of the immunoglobulin gene

The genomic DNA from PBMCs was extracted by using the QIAamp DNA Micro Kit (Qiagen, Hilden, Germany). The upstream flanking region to the highly repetitive Smu core region was amplified with *PfuTurbo* DNA polymerase (Stratagene, La Jolla, Calif) and the following primers (Fig 1): Imu-1S, 5′-AGATTCTGTTCCGAATCACCGATG-3′; and Smu-1AS, 5′-CCATCTGAGTCCATTTCTGA-3′. A 1128-bp fragment was sequenced from position 12,880 to position 13,794 of NT_010168.8. Within this region, the G/C content and the RGYW/WRCY (W, A/T; R, A/G; and Y, C/T) motifs are equally distributed, as shown in Fig 1.

The GeneAmp PCR System 9700 (Applied Biosystems, Foster City, Calif) was used for the PCR reaction by using the following temperature program: 40 cycles of 95°C for 30 seconds, 60°C for 30 seconds, and 72°C for 2 minutes. After the PCR products were subcloned with the Topo TA cloning kit for Sequencing (Invitrogen, Carlsbad, Calif), the plasmid was extracted by using Perfectprep Plasmid 96Vac Direct Bind (Eppendorf AG, Hamburg, Germany). The sequencing reaction of the obtained plasmid was conducted by using the BigDye Terminator V1.1 cycle sequencing kit (Applied Biosystems) and analyzed with Genetic analyzer 3130XL (Applied Biosystems). More than 18 unique clones (20,304 bases) were analyzed for each control.

In vitro induction of SHM in Smu-SHM in control B cells after CSR activation

PBMCs were separated by means of Ficoll-Hypaque density centrifugation with Lymphoprep (Axis-Shied PoC) and were cultured at a final concentration of 2.0×10^6 cells per milliliter under standard conditions (37°C and 5% CO_2) in RPMI 1640 medium (Invitrogen) containing 10% heat-inactivated FCS (Invitrogen), penicillin (100 U/mL), streptomycin (100 μg/mL; Cellgro, Manassas, Va), anti-CD40–stimulating mAb (anti-CD40 mAb; G28-5, 1 μg/mL), and recombinant IL-4 (100 U/mL; R&D Systems, Minneapolis, Minn). The induction of AID expression was confirmed by means of relative quantification with TaqMan Gene Expression Assays (Applied Biosystems) with a 7300 Fast Real Time PCR System (Applied Biosystems, data not shown). The genomic DNA from B cells was extracted, and the presence of Smu-SHM was analyzed as described above.

In vivo detection of SHM in the switch region of IgM in control subjects and CD40L-, AID-, and UNG-deficient patients

B cells were purified from the peripheral blood of 4 control subjects (C1-C4) by using the RosetteSep Human B Cell Enrichment Cocktail (StemCell Technologies, Vancouver, British Columbia, Canada). The enriched B cells (>90% purity) were stained with anti-IgM–phycoerythrin-Cy5 (BD Biosciences, San Jose, Calif), anti-CD19–allophycocyanin, anti-CD27–phycoerythrin, and anti-IgD–fluorescein isothiocyanate (Beckman Coulter, Fullerton, Calif), according to the manufacturer's suggestions. The $CD19^+$ cells were gated, and the $IgD^+IgM^+CD27^-$, $IgD^+IgM^+CD27^+$, and $IgD^-IgM^-CD27^+$ cells were sorted by using FACSVantage (BD Biosciences). The mean purities of these fractions were 95.6%, 86.9%, and 94.8%, respectively. Because of the absence of class-switched B cells ($IgD^-IgM^-CD27^+CD19^+$) in immunoglobulin CSR–deficient patients (P1-P11), we purified only the $CD27^+$ and $CD27^-$ fractions from the B cells of these patients and their age-matched control subjects (C5-C7, >90% purity). The genomic DNA from the B cells was extracted, and the presence of the switch region of IgM (Smu-SHM) was analyzed, as described above.

RESULTS

In vitro induction of SHM in Smu-SHM in human B cells following CSR activation

To examine whether Smu-SHMs are indeed linked to the induction of CSR in human B cells, we stimulated the PBMCs of control subjects (C1-C4) with anti-CD40 mAb and IL-4, which is a combination that powerfully stimulates the induction of *in vitro* CSR, but not V-SHM,[13,14] in human B cells. This stimulation, as reported previously, induced AID expression, functional transcripts of IgE (as determined by using RT-PCR), and IgE production (as determined by using ELISA) in the supernatants of all (C1-C4) human B-cell cultures (data not shown).

The unstimulated PBMCs presented very few Smu-SHMs (0.006% ± 0.004% bp, mean ± SD; Fig 2, *A*). On CSR-inducing anti-CD40 mAb and IL-4 stimulation, the Smu-SHM frequency significantly increased (0.045% ± 0.002% bp, $P = .0361$). The induced Smu-SHMs were equally targeted to GC and AT (the GC target was 47.4%). The transition type of the mutations was increased at the G and C nucleotides (GC transition, 72.2%) but was not altered at the A and T nucleotides (AT transition,

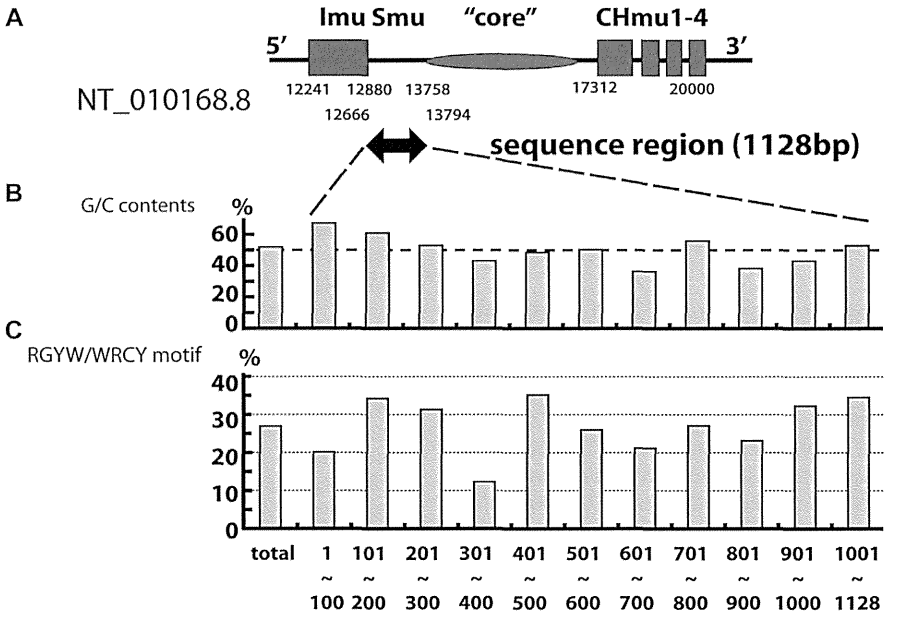

FIG 1. Sequence region for the analysis of mutations in Smu-SHM. **A,** We amplified, subcloned, and sequenced the 5′ region of the highly repetitive GC-rich region of the IgM gene (Smu core) using Pfu polymerase. **B,** Percentages of G and C nucleotides (G/C contents) are equally distributed throughout the sequence region. **C,** Percentages of RGYW/WRCY motifs in each 100-bp fragment are not significantly different throughout the sequence region. *CHmu1-4,* Exons of the constant region of IgM; *Imu,* enhancer exon of the IgM gene; *R,* purines (A/G); *W,* A/T; *Y,* pyrimidines (C/T).

50.0%; Fig 2, *B*). In contrast, the VH-SHMs at the JH4-JH5 region were not changed because of stimulation (Fig 2, *A*). These results indicate that Smu-SHMs can be induced *in vitro* by means of CSR activation.

In vivo induction of Smu-SHM in human B cells

We separated human B cells into 3 subpopulations (naive B cells, unswitched memory B cells, and switched memory B cells) using fluorescence-activated cell sorting based on the expression of IgM, IgD, CD27, and CD19[15] from the PBMCs of healthy adults (n = 4; Fig 3, *A*). We purified the genomic DNA from each purified B-cell subpopulation and amplified the Smu region (5′ to the Smu core region containing repetitive sequences) with the high-fidelity *Pfu* DNA polymerase and Smu-specific primers (Fig 1, *A*).

We found that the frequency of Smu-SHMs in the $IgD^-IgM^-CD27^+$ switched memory B cells was 20-fold higher (0.21% ± 0.014% bp) than that found in the $IgD^+IgM^+CD27^-$ naive B cells (0.008% ± 0.003% bp, $P < .001$). The frequency of Smu-SHMs in the $IgD^+IgM^+CD27^+$ unswitched memory B cells (0.13% ± 0.023% bp) was also significantly higher than that found in naive B cells ($P < .001$) and significantly lower than that found in switched memory B cells ($P < .001$; Fig 3, *B*). The mutations were mainly point mutations (Fig 3, *C*), but some small deletions were also observed in each fraction (Table I).

Distribution of Smu-SHMs within the 5′ upstream region of Smu core

We then compared the frequency of SHMs among the 1- to 400-bp, 401- to 800-bp, and 801- to 1128-bp regions of the 5′ upstream region of the Smu core region.

In all 5′ regions (1-400 bp, 401-800 bp, and 801-1128 bp), the switched memory B-cell subpopulation exhibited a significantly higher frequency of SHMs than the unswitched memory and naive B cells (Fig 4).

In the 1- to 400-bp region (Fig 4, *A*), which is the most distant from the Smu core region, the SHM frequencies found in the unswitched memory and naive B cells were not significantly different. However, the switched memory B cells (0.15% ± 0.05% bp) presented a higher frequency of SHMs than the unswitched memory B cells (0.06% ± 0.04% bp, $P < .05$) and naive B cells (0.00% ± 0.00% bp, $P < .001$).

In the 401- to 800-bp region (Fig 4, *B*) the switched memory B cells (0.19% ± 0.02% bp) exhibited a significantly higher frequency of SHMs than the unswitched memory B cells (0.07% ± 0.03% bp, $P < .001$) and naive B cells (0.01% ± 0.01% bp), and the unswitched memory B cells presented a higher frequency of SHMs than the naive B cells ($P < .01$).

In the 801- to 1128-bp region (Fig 4, *C*), which is the closest to the Smu core region, both switched (0.29% ± 0.02% bp) and unswitched (0.27% ± 0.05% bp) memory B-cell subpopulations exhibited significantly higher SHM frequencies than naive B cells (0.02% ± 0.02% bp, $P < .001$). The SHM frequencies obtained for the switched and unswitched memory B cells were not significantly different.

These differences were independent of the distributions of G and C nucleotides (Fig 1, *B*) and WRCY/RGYW motifs (Fig 1, *C*) because these motifs are equally distributed in these regions.

Sequence analysis of Smu-SHMs in memory B cells

The Smu region analyzed in this study (1128 bp) contains 40 WRCY motifs (160 bp, 14.2% of the length of the Smu region)

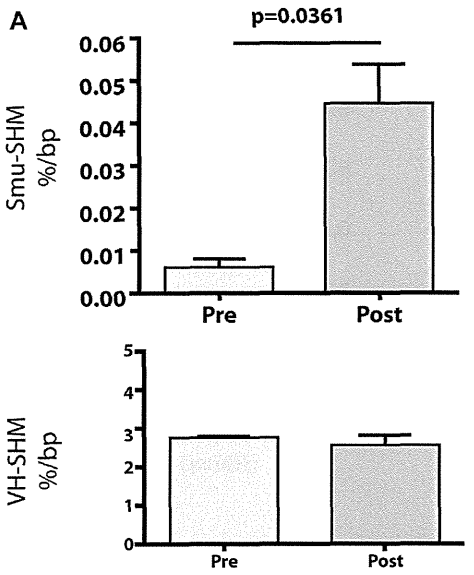

B

from \ to	A	C	G	T	sum
A		2	5	3	10
C	1		0	6	7
G	7	2		2	11
T	4	5	1		10

GC target	47.4%
GC transition	72.2%
AT transition	50.0%

FIG 2. Smu-SHMs induced by anti-CD40 mAb and IL-4 *in vitro* in PBMCs of the control subjects. **A,** Smu-SHMs were analyzed before and after stimulation of PBMCs from control subjects (n = 4) with anti-CD40 mAb and IL-4 for 5 days *in vitro*. Mutations were rarely found before stimulation (*Pre,* 0.006% ± 0.004% bp) but were significantly increased after stimulation with anti-CD40 mAb and IL-4 *in vitro* (*Post,* 0.04% ± 0.02% bp, $P = .0361$). The VH-SHMs at the JH4-JH5 region were analyzed, but no significant difference was observed because of stimulation. **B,** The Smu-SHM pattern observed after stimulation with anti-CD40 mAb and IL-4 is shown. The germline nucleotides are shown on the left *(from),* and the mutated nucleotides are shown on the top *(to).* The *right column* indicates the sum of the mutated nucleotides for each row. The *GC target* indicates the mutations at G or C. The *GC transition* indicates the frequency of transition mutations at G and C (G>A and C>T) of the total mutations at G and C. The *AT transition* indicates the frequency of transition mutations at A and C (A>G and T>C) of the total mutations at A and T.

and 43 RGYW motifs (172 bp, 15.2% of the length of the Smu region). In addition, 73.0% of the region is independent of either of the 2 motifs (824 bp, Fig 5).

We found 18 (unswitched memory B cells) and 41 (switched memory B cells) mutations in the WRCY motifs, which correspond to 1.12- and 1.35-fold increases in mutations compared with the expected number, respectively. Similar to the findings obtained in the analysis of the WRCY motif, we found 26 and 64 mutations in the RGYW motif, which correspond to 1.51- and 1.97-fold more mutations than expected, respectively. Thus Smu-SHMs tended to be observed within the WRCY/RGYW motifs. The C nucleotide was the preferential target in the WRCY motif because this nucleotide was the target in 52% and 51% of the mutations that were observed in unswitched memory and switched memory B cells, respectively. The G nucleotide was preferentially targeted in the RGYW motifs because it was the target in 50% and 51% of the mutations observed in unswitched memory and switched memory B cells, respectively. Outside the WRCY/RGYW motifs, the A and T nucleotides were predominantly mutated in both switched (60%) and unswitched (62%) memory B cells. The mutations at A were as frequent as those at T. In unswitched memory B cells 75.6% of the mutations at A/T were found within the WA/TW motifs, and WA/TW to WG/TC mutations accounted for 52.9% of the mutations in WA/TW motifs. In switched memory B cells 55.7% of the mutations at A/T were found within the WA/TW motifs, and WA/TW to WG/TC mutations accounted for 43.6% of the mutations in WA/TW motifs.

Smu-SHM in CD40L-, AID-, and UNG-deficient patients

To assess the CD40L, AID, and UNG dependency of the CSR process in human B cells, we analyzed the Smu-SHMs in peripheral blood purified B cells from age-matched control subjects (C1-C7) and 5 AID-deficient (P1-P5), 2 UNG-deficient (P6 and P7), and 4 CD40L-deficient (P8-P11) patients. There was no significant difference in the frequency of Smu-SHMs in $CD27^+$ memory B cells from control adults (C1-C4) and control children (C5-C7; Fig 6, *A*).

The frequencies of Smu-SHM were decreased, and small deletions were not observed (Table I) in both $CD27^+$ and $CD27^-$ B cells (Fig 6, *A*, and data not shown) in the AID- and CD40L-deficient patients, indicating the dependence of Smu-SHM on AID and CD40L. The mutation pattern of the CD40L-deficient patients was not significantly different from that of the control subjects (Fig 6, *B*). Of the 2 UNG-deficient patients,[2] P6, who has a homozygous missense mutation, presented a significantly decreased frequency of Smu-SHMs in both $CD27^+$ and $CD27^-$ B cells, and P7, who has homozygous 2-bp deletions, exhibited an increased Smu-SHM frequency in $CD27^+$ B cells but a decreased frequency in $CD27^-$ B cells (Fig 6, *A*, and data not shown). This discrepancy cannot be related to the patient's age because no difference in the Smu-SHM frequency was observed according to age (Fig 6, *A*). None of the UNG-deficient patients had small deletions in the Smu region (Table I). An important finding is that Smu-SHMs exhibited significant and characteristic bias to transitions at G and C nucleotides in both patients

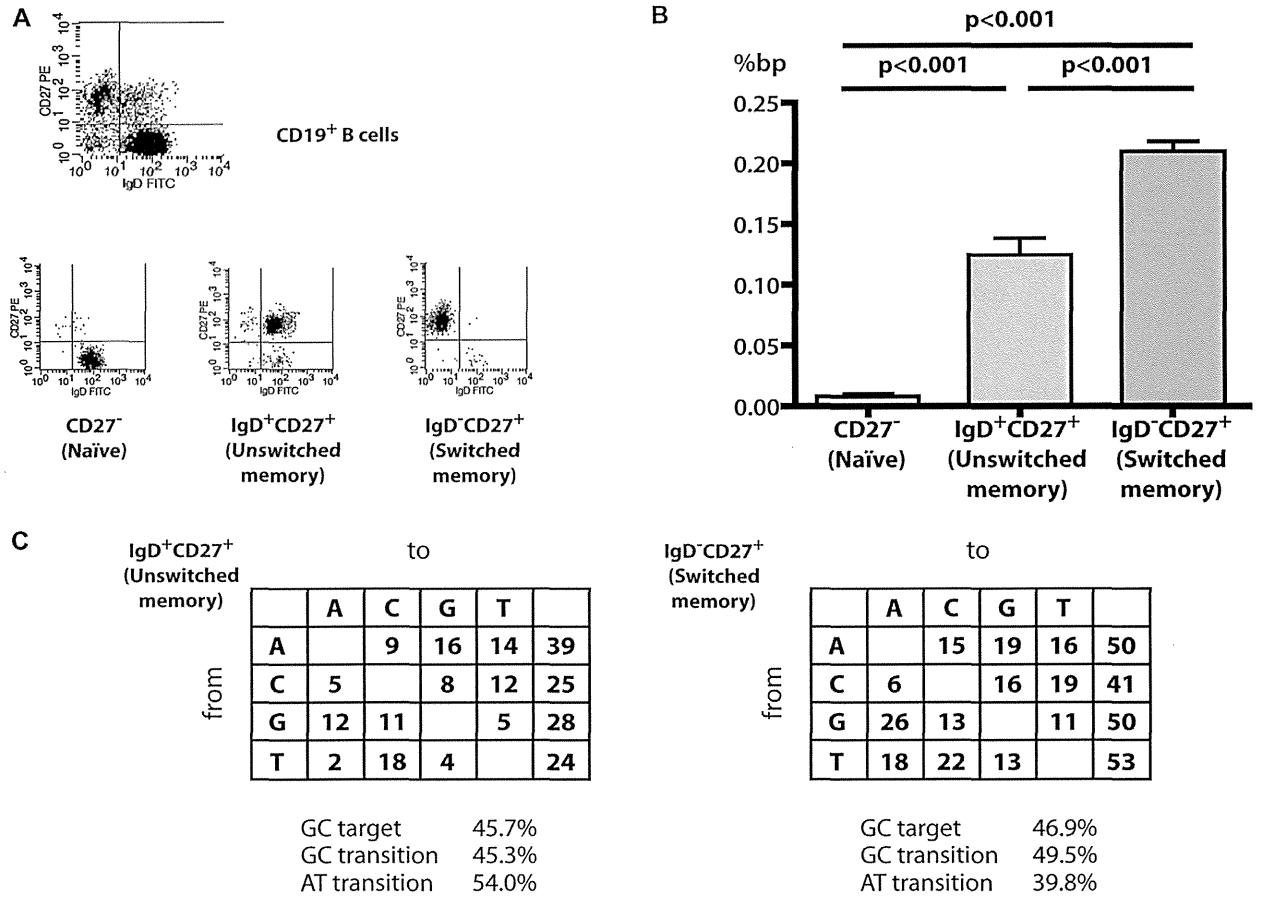

from \ to	A	C	G	T	
A		9	16	14	39
C	5		8	12	25
G	12	11		5	28
T	2	18	4		24

from \ to	A	C	G	T	
A		15	19	16	50
C	6		16	19	41
G	26	13		11	50
T	18	22	13		53

FIG 3. *In vivo* Smu-SHMs in control subjects. **A,** We purified $IgD^+IgM^+CD27^-$ (naive), $IgD^+IgM^+CD27^+$ (unswitched memory), and $IgD^-IgM^-CD27^+$ (switched memory) B cells from control subjects (n = 4) using fluorescence-activated cell sorting. Representative fluorescence-activated cell sorting data are shown. **B,** We found a higher frequency of Smu-SHMs in $IgD^-IgM^-CD27^+$ B cells, which are class-switched, and V region–mutated B cells, than in $IgD^+IgM^+CD27^+$ B cells, which are V region mutated but not class-switched B cells. The $IgD^+IgM^+CD27^-$ (naive) B cells presented the lowest frequency of Smu-SHMs. **C,** The mutation patterns of unswitched *(left)* and switched *(right)* memory B cells are shown.

(Fig 6, *B*). In contrast, A/T-targeted mutations were observed in P7, similarly to the control subjects. These results demonstrate the contribution of UNG to the formation of Smu-SHMs during CSR.

DISCUSSION

We demonstrated that SHMs occur in the Smu region in not only *in vivo* CSR-induced human B cells but also B cells activated *in vitro* with anti-CD40 mAb and IL-4, a combination that induces AID expression and CSR but not V-SHM.[14] Because the V and S regions are both transcribed on stimulation, the discrepancy between V-SHM and S-SHM occurrence *in vitro* might be related to the R-loop structure of the S (but not V) region, likely because of differences in G/C content or secondary structure.[8]

In fact, we found a significant amount of mutations in the Smu region of switched memory B cells. This amount was more than 4-fold higher than the frequency observed in B cells stimulated *in vitro*. We also found that unswitched memory B cells presented more Smu-SHMs than naive B cells, suggesting that the unswitched memory B-cell subpopulation contains a fraction that has unsuccessfully undergone CSR after the introduction of AID deamination and error-free DNA repair. These results indicate that Smu-SHMs are closely associated with CSR both *in vivo* and *in vitro* and suggest that Smu-SHMs precede the completion of CSR.

We observed significantly more mutations in the 3′ part than the 5′ part of the Smu region, even though the distribution of all of the nucleotides and the WRCY/RGYW motifs are equivalent throughout the region. Although the sequenced region is outside of the Smu core region with highly repetitive, G/C-rich sequences, this region is also known to form the R-loop with single-stranded DNA and a DNA-RNA hybrid.[16] As observed in the Smu core region, this R-loop structure might allow the accessibility of DNA to AID-induced deamination. The preferential targeting of Smu-SHMs to the 3′ part of the Smu region might reflect the frequency of the deamination of AID during CSR. Furthermore, we found more Smu-SHMs in the 5′ part of the Smu region of $IgD^-IgM^-CD27^+$ class-switched memory B cells than in the Smu region of $IgD^+IgM^+CD27^+$ unswitched memory B cells

TABLE I. *In vivo* Smu-SHMs in control subjects and patients

		$IgD^+IgM^+CD27^+$ (unswitched memory)						$IgD^-IgM^-CD27^+$ (switched memory)					
		Total clones	Mutated clones	Percentage	Clones with small deletions	Percentage	Length of small deletions (bp)	Total clones	Mutated clones	Percentage	Clones with small deletions	Percentage	Length of small deletions (bp)
C1	Adult control subjects	23	5	22	1	20	1	21	15	71	2	13	30, 72
C2		21	8	38	3	38	1, 1, 11	21	15	71	1	7	1
C3		19	7	37	1	14	8	20	10	50	1	10	5
C4		21	11	52	0	0	—	21	14	67	1	7	8, 28
				$CD27^+$									
C5	Age-matched control subjects	18	5	28	0	0	—						
C6		19	11	58	0	0	—						
C7		19	8	42	4	50	2, 11, 12, 25						
P1	AID deficiency	22	2	9	0	0	—						
P2		18	0	0	0	0	—						
P3		21	3	14	0	0	—						
P4		11	0	0	0	0	—						
P5		13	0	0	0	0	—						
P6	UNG deficiency	34	4	12	0	0	—						
P7		20	17	85	0	0	—						
P8	CD40L deficiency	20	10	50	0	0	—						
P9		20	3	15	0	0	—						
P10		23	1	4	0	0	—						
P11		22	4	18	0	0	—						

The genomic DNA from the purified unswitched memory and switched memory B cells of adult control subjects (C1-C4) and $CD27^+$ memory B cells from age-matched control subjects (C5-C7) and patients with AID (P1-P5), UNG (P6-P7), and CD40L (P8-P11) deficiency was analyzed for Smu-SHMs. *Total clones* indicates analyzed clones. *Mutated clones* indicates clones with at least 1 mutation. The percentage indicates the proportion of mutated clones in the total clones. The number and proportion of clones with small deletions are also shown. The length of small deletions (in base pairs) is indicated for each subject.

(Fig 3, *A*). This finding might suggest that the R-loop extension in the 5′ region of the S region contributes to CSR by opening the chromatin structure of this region to allow access for AID (see Fig E1 in this article's Online Repository at www.jacionline.org).[16] The R-loop is a characteristic structure of the S region. Our observation is consistent with the finding that the R-loop is wider in the 5′ region than formerly considered. This widespread R-loop formation might be important for CSR by opening the chromatin structure or some other unknown mechanism. These results indicate that Smu-SHMs start in the 3′ region and then spread to the 5′ upstream region during the CSR phase and that the R-loop might be larger in switched memory B cells than unswitched and naive B cells (see Fig E1). Thus the switched memory cells might have more chance of successful CSR than unswitched memory and naive B cells. Further study is needed to analyze the R-loop formation in the S region during the CSR stimulation by using the bisulfite modification assay[16] to prove this hypothesis.

We compared the nucleotide mutation pattern of Smu-SHMs with that of V-SHMs in memory B cells and found that the mutations at A were as frequent as those at T in the Smu-SHM both *in vivo* and *in vitro* (Figs 2, *C*, and 6, *B*). This finding for Smu-SHMs is different from that observed for V-SHMs because the frequency of V-SHMs at A residues is 2-fold higher than that found for T residues.[17] Smu-SHMs at A and T residues are dependent on MMR and the DNA polymerase eta.[18,19] In V-SHM the preference of A residues over T residues is explained by the preference for MMR molecules on the top strand of opened double-stranded DNA.[20] Our results might suggest that AID deamination and MMR contribute equally to both the top and bottom strands of the S region, which is different from the findings found for the V region and characteristic for Smu-SHMs. Because the number of mutations analyzed in this study is limited, further studies using next-generation sequencing would be helpful to elucidate these questions.[21]

We found that Smu-SHMs at C and G were limited within WRCY and RGYW motifs, respectively, whereas mutations at A and T were observed outside of these motifs *in vivo* (Fig 4). Because WRCY/RGYW motifs are known as target motifs of SHM in the V region and as a target sequence of RPA-binding phosphorylated AID,[22] this result indicates that AID is involved in Smu-SHMs, as well as V-SHMs, by inducing deamination on Smu-SHM in human B cells *in vivo*.

Stimulation with anti-CD40 mAb and IL-4, which induces Smu-SHM, does not induce V-SHM. This discrepancy might be due to the R-loop formation in the Smu region but not in the V region on stimulation *in vitro*. AID favors the single-strand DNA observed in the R-loop of Smu region, which is not formed in V regions by CSR stimulation.

To further investigate the roles of CD40L, AID, and UNG in Smu-SHMs in human B cells, we studied the B-cell subpopulations (naive and memory) from CD40L-deficient (n = 4), AID-deficient (n = 5), and UNG-deficient (n = 2) patients. The results show that Smu-SHMs were reduced in both CD40L- and AID-deficient patients, even in their $CD27^+$ B cells. This observation, which demonstrates the essential role for AID in Smu-SHM generation, similarly to that observed in V-SHM,[1] confirms data previously reported for successfully recombined Smu regions from unseparated peripheral blood B-cell populations of patients with heterozygous dominant negative AID mutations.[10]

The analysis of the UNG-deficient patients showed that the Smu-SHM frequency was decreased in one patient (P6) but increased in the other patient (P7). Because both patients lack expression of the UNG protein,[2,23] this discrepancy could not be explained by their different genotypes. In addition, the difference

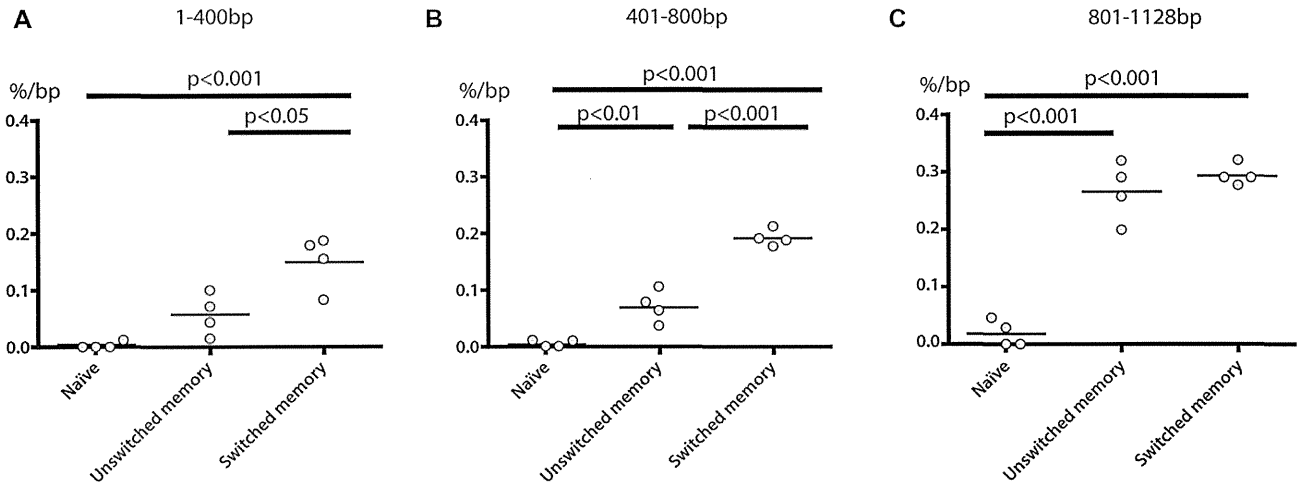

D

	Nucleotide number		
	1-400	401-800	801-1128
Naïve ($IgD^+IgM^+CD27^-$)	0.00±0.00	0.01±0.01	0.02±0.02
Unswitched memory ($IgD^+IgM^+CD27^+$)	0.06±0.04	0.07±0.03	0.27±0.05
Switched memory ($IgD^-IgM^-CD27^+$)	0.15±0.05	0.19±0.02	0.29±0.02

FIG 4. Distribution of Smu-SHMs in each fraction of control B cells *in vivo*. **A-C,** The frequency of Smu-SHMs was higher in the 3′ region than in the 5′ region in both IgD^- (switched) and IgD^+ (unswitched) fractions of $CD27^+$ B cells. **D,** Means ± SDs of Smu-SHMs in each region are shown (n = 4).

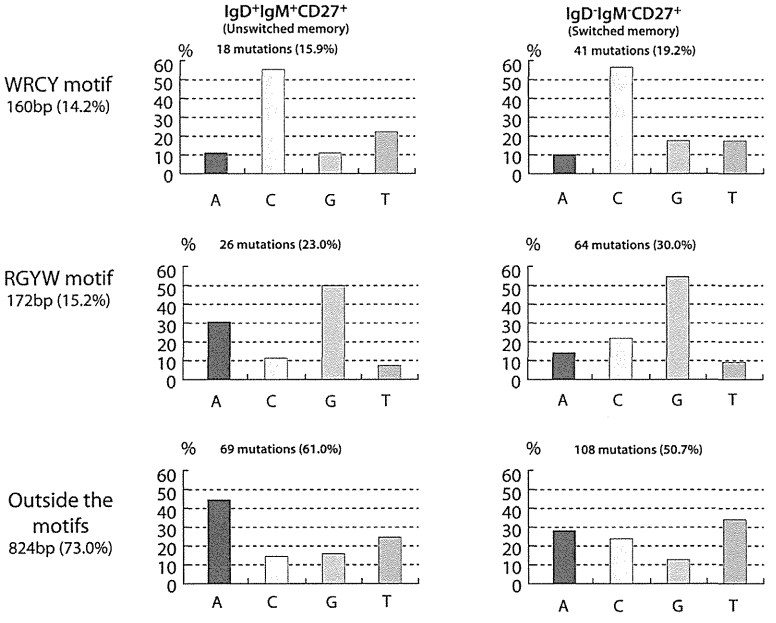

FIG 5. Target motifs of Smu-SHMs in each fraction of control B cells *in vivo*. The Smu-SHMs of the control subjects *in vivo* (n = 4) were analyzed according to their target motifs in each fraction of B cells ($IgD^+IgM^+CD27^+$ and $IgD^-IgM^-CD27^+$ B cells). *R,* Purines (A/G); *W,* A/T; *Y,* pyrimidines (C/T).

does not appear to be related to age because we did not observe any discrepancy between B cells from children and adult control subjects (Fig 6, *A*). Neither of the 2 UNG-deficient patients had small deletions in the Smu region. Smu-SHMs exhibited a skewed pattern similar to that seen in V-SHM[2] (ie, an excess of transitions on G and C nucleotides [G to A, 100%; C to T, 98.4%]) and an

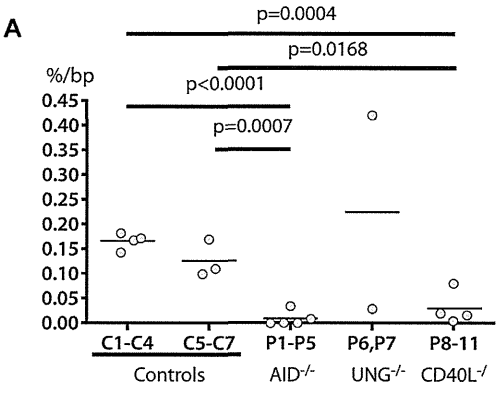

B

C1-C4 (control adults)

from \ to	A	C	G	T	
A		24	35	30	89
C	11		24	31	66
G	38	24		16	78
T	20	40	17		77

GC target 46.5%
GC transition 47.9%
AT transition 45.2%

C5-C7 (control children)

from \ to	A	C	G	T	
A		6	10	8	24
C	1		4	8	13
G	20	8		1	29
T	6	7	2		15

GC target 51.9%
GC transition 66.7%
AT transition 43.6%

P6,7 (UNG-/-)

from \ to	A	C	G	T	
A		4	8	6	18
C	1		0	28	29
G	45	0		0	45
T	4	8	2		14

GC target 69.8%
GC transition 98.6%
AT transition 50.0%

P8-11 (CD40L-/)

from \ to	A	C	G	T	
A		2	3	2	7
C	0		1	2	3
G	9	3		2	14
T	1	2	0		3

GC target 63.0%
GC transition 64.7%
AT transition 50.0%

FIG 6. Smu-SHMs in patients with CD40L, AID, and UNG deficiency *in vivo*. **A,** Smu-SHMs in the CD27$^+$ fraction of B cells from control adults (C1-C4), control children (C5-C7), and AID-deficient (P1-P5), UNG-deficient (P6 and P7), and CD40L-deficient (P8-11) patients. The frequency of Smu-SHMs was decreased in patients with AID (P1-P5) and CD40L (P8-11) deficiency. In patients with UNG deficiency, the Smu-SHM frequency was decreased in P6 but increased in P7. **B,** The mutations were significantly targeted and biased to transition at G and C in UNG-deficient patients (P6 and P7).

increased targeting of G and C in both patients. This result indicates that in the absence of UNG, CSR-induced AID-dependent deaminated cytidines on both strands of the S region lead to transition mutations during their replications.

In contrast, we found normal mutation patterns at A and T in both UNG-deficient patients. The U/G mismatch introduced by AID in the S region, similarly to that observed in the V region, can be recognized by the MMR pathway. The MMR, particularly the MSH2/MSH6 complex, has been shown to be essential in the absence of UNG for both CSR and SHM in mice.[11,19] The MLH1/PMS2 complex is also reported to be important for CSR.[24] MMR deficiencies (PMS2 and MSH6 biallelic mutations) are associated with mild CSR deficiency in human subjects.[25,26] In the V regions the recruitment of the DNA polymerase eta (POLH) by the MSH2/MSH6 complex is responsible for mutations on A/T residues.[27] However, this alternative pathway, which compensates for UNG deficiency in V-SHM and Smu-SHM, is not sufficient in human subjects to induce full CSR, as shown by the marked immunoglobulin CSR deficiency and the complete lack of small deletions in Smu regions observed in both patients. In the absence of UNG, CSR-induced AID-dependent lesions in the S regions lead to mutations occurring during their repair but are inefficient for the generation of the double-strand DNA breaks necessary for CSR in human subjects.

At present, most of the hyper-IgM syndromes caused by an intrinsic B-cell defect remain molecularly undefined.[28,29] An analysis of the frequency and occurrence of CSR-induced Smu-SHMs might be a useful tool to better understand the molecular defect in these patients and disclose the CSR mechanisms.

We thank Dr Ritsuo Nishiuchi (Kochi Health Sciences Center, Kohchi, Japan) for taking care of the patients and Ms Makiko Tanaka (National Defense Medical College, Saitama, Japan) and Ms Monique Forveille (U768, INSERM, Paris, France) for their skillful technical assistance. We also thank the critical reading performed by Dr Patrick Revy (U768, INSERM, Paris, France).

Key messages

- **CSR-induced mutations occurring in Smu-SHM were observed in both *in vitro* and *in vivo* switched and unswitched human memory B cells.**
- **The extension of SHM to the 5′ upstream region of Smu might be associated with the effective induction of CSR.**
- **Smu-SHM depends on CD40L, AID, UNG, and the MMR system.**

REFERENCES

1. Revy P, Muto T, Levy Y, Geissmann F, Plebani A, Sanal O, et al. Activation-induced cytidine deaminase (AID) deficiency causes the autosomal recessive form of the hyper-IgM syndrome (HIGM2). Cell 2000;102:565-75.
2. Imai K, Slupphaug G, Lee W-I, Revy P, Nonoyama S, Catalan N, et al. Human uracil-DNA glycosylase deficiency associated with profoundly impaired immunoglobulin class-switch recombination. Nat Immunol 2003;4:1023-8.
3. Durandy A, Revy P, Imai K, Fischer A. Hyper-immunoglobulin M syndromes caused by intrinsic B-lymphocyte defects. Immunol Rev 2005;203:67-79.
4. Yan CT, Boboila C, Souza EK, Franco S, Hickernell TR, Murphy M, et al. IgH class switching and translocations use a robust non-classical end-joining pathway. Nature 2007;449:478-82.

5. Chaudhuri J, Alt FW. Class-switch recombination: interplay of transcription, DNA deamination and DNA repair. Nat Rev Immunol 2004;4:541-52.
6. Nagaoka H, Muramatsu M, Yamamura N, Kinoshita K, Honjo T. Activation-induced deaminase (AID)-directed hypermutation in the immunoglobulin Smu region: implication of AID involvement in a common step of class switch recombination and somatic hypermutation. J Exp Med 2002;195:529-34.
7. Schrader CE, Vardo J, Stavnezer J. Mlh1 can function in antibody class switch recombination independently of Msh2. J Exp Med 2003;197:1377-83.
8. Peled JU, Kuang FL, Iglesias-Ussel MD, Roa S, Kalis SL, Goodman MF, et al. The biochemistry of somatic hypermutation. Annu Rev Immunol 2008;26:481-511.
9. Muramatsu M, Kinoshita K, Fagarasan S, Yamada S, Shinkai Y, Honjo T. Class switch recombination and hypermutation require activation-induced cytidine deaminase (AID), a potential RNA editing enzyme. Cell 2000;102:553-63.
10. Kracker S, Imai K, Gardës P, Ochs HD, Fischer A, Durandy AH. Impaired induction of DNA lesions during immunoglobulin class-switch recombination in humans influences end-joining repair. Proc Natl Acad Sci U S A 2010;107:22225-30.
11. Xue K, Rada C, Neuberger MS. The in vivo pattern of AID targeting to immunoglobulin switch regions deduced from mutation spectra in msh2-/- ung-/- mice. J Exp Med 2006;203:2085-94.
12. Zhu Y, Nonoyama S, Morio T, Muramatsu M, Honjo T, Mizutani S. Type two hyper-IgM syndrome caused by mutation in activation-induced cytidine deaminase. J Med Dent Sci 2003;50:41-6.
13. Fecteau JF, Néron S. CD40 stimulation of human peripheral B lymphocytes: distinct response from naive and memory cells. J Immunol 2003;171:4621-9.
14. Nonoyama S, Hollenbaugh D, Aruffo A, Ledbetter JA, Ochs HD. B cell activation via CD40 is required for specific antibody production by antigen-stimulated human B cells. J Exp Med 1993;178:1097-102.
15. Warnatz K, Denz A, Dräger R, Braun M, Groth C, Wolff-Vorbeck G, et al. Severe deficiency of switched memory B cells (CD27(+)IgM(-)IgD(-)) in subgroups of patients with common variable immunodeficiency: a new approach to classify a heterogeneous disease. Blood 2002;99:1544-51.
16. Huang F-T, Yu K, Balter BB, Selsing E, Oruc Z, Khamlichi AA, et al. Sequence dependence of chromosomal R-loops at the immunoglobulin heavy-chain Smu class switch region. Mol Cell Biol 2007;27:5921-32.
17. Neuberger MS, Noia JMD, Beale RCL, Williams GT, Yang Z, Rada C. Somatic hypermutation at A·T pairs: polymerase error versus dUTP incorporation. Nat Rev Immunol 2005;5:171-8.
18. Faili A. DNA polymerase is involved in hypermutation occurring during immunoglobulin class switch recombination. J Exp Med 2004;199:265-70.
19. Rada C, Di Noia JM, Neuberger MS. Mismatch recognition and uracil excision provide complementary paths to both Ig switching and the A/T-focused phase of somatic mutation. Mol Cell 2004;16:163-71.
20. Unniraman S, Schatz DG. Strand-biased spreading of mutations during somatic hypermutation. Science 2007;317:1227-30.
21. Perez-Duran P, Belver L, de Yebenes VG, Delgado P, Pisano DG, Ramiro AR. UNG shapes the specificity of AID-induced somatic hypermutation. J Exp Med 2012;209:1379-89.
22. Chaudhuri J, Khuong C, Alt FW. Replication protein A interacts with AID to promote deamination of somatic hypermutation targets. Nature 2004;430:992-8.
23. Kavli B, Andersen S, Otterlei M, Liabakk NB, Imai K, Fischer A, et al. B cells from hyper-IgM patients carrying UNG mutations lack ability to remove uracil from ssDNA and have elevated genomic uracil. J Exp Med 2005;201:2011-21.
24. Chahwan R, van Oers JMM, Avdievich E, Zhao C, Edelmann W, Scharff MD, et al. The ATPase activity of MLH1 is required to orchestrate DNA double-strand breaks and end processing during class switch recombination. J Exp Med 2012;209:671-8.
25. Péron S, Metin A, Gardës P, Alyanakian M-A, Sheridan E, Kratz CP, et al. Human PMS2 deficiency is associated with impaired immunoglobulin class switch recombination. J Exp Med 2008;205:2465-72.
26. Gardës P, Forveille M, Alyanakian M-A, Aucouturier P, Ilencikova D, Leroux D, et al. Human MSH6 deficiency is associated with impaired antibody maturation. J Immunol 2012;188:2023-9.
27. Delbos F, Aoufouchi S, Faili A, Weill J-C, Reynaud C-A. DNA polymerase eta is the sole contributor of A/T modifications during immunoglobulin gene hypermutation in the mouse. J Exp Med 2007;204:17-23.
28. Imai K, Catalan N, Plebani A, Maródi L, Sanal O, Kumaki S, et al. Hyper-IgM syndrome type 4 with a B lymphocyte-intrinsic selective deficiency in Ig class-switch recombination. J Clin Invest 2003;112:136-42.
29. Péron S, Pan-Hammarström Q, Imai K, Du L, Taubenheim N, Sanal O, et al. A primary immunodeficiency characterized by defective immunoglobulin class switch recombination and impaired DNA repair. J Exp Med 2007;204:1207-16.

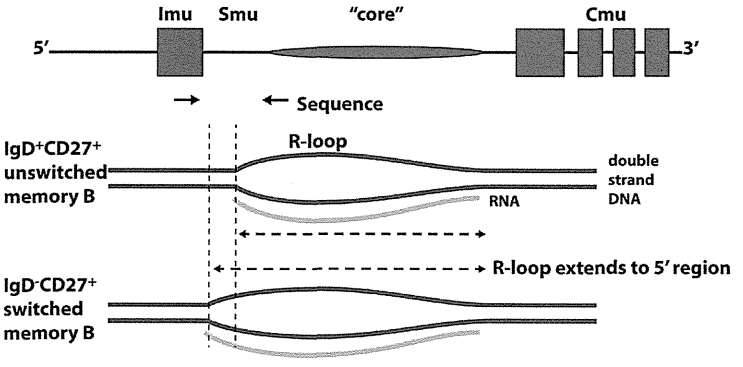

FIG E1. Smu-SHMs might correspond to the extension of the R-loop. We found more mutations in the 3′ part of the sequenced region, which is close to the Smu core region, than in the 5′ region in both unswitched and switched memory B cells. Furthermore, we found more mutations in the 5′ part of the sequenced region in switched memory B cells than in unswitched memory B cells. These findings might indicate the extension of the R-loop during CSR.

Molecular Genetics and Metabolism 112 (2014) 154–159

Contents lists available at ScienceDirect

Molecular Genetics and Metabolism

journal homepage: www.elsevier.com/locate/ymgme

CT and endoscopic evaluation of larynx and trachea in mucopolysaccharidoses

Noriko Morimoto [a,*], Masayuki Kitamura [b], Motomichi Kosuga [c], Torayuki Okuyama [c]

[a] Department of Otolaryngology, National Center for Child Health and Development, Japan
[b] Department of Radiology, National Center for Child Health and Development, Japan
[c] Center for Lysosomal storage diseases, National Center for Child Health and Development, Japan

ARTICLE INFO

Article history:
Received 25 January 2014
Received in revised form 27 March 2014
Accepted 27 March 2014
Available online 4 April 2014

Keywords:
GAG deposit
Morphology
Endoscopy
CT
Tracheal cross-sectional surface area

ABSTRACT

Background: Mucopolysaccharidoses (MPSs) are lysosomal storage disorders caused by lysosomal enzyme deficiencies that result in systemic accumulation of glycosaminoglycans (GAGs). Accumulation of GAGs in the upper airway can lead to respiratory failure. The aim of this study was to investigate changes of the airway by flexible endoscopy and CT.
Methods: Thirty-five patients aging from 2 to 16 years (mean: 9.2 ± 4.4 years) participated in this study. The majority had MPS I (n = 5) or MPS II (n = 25). The shape of the trachea and the cross-sectional trachea surface area (TSA) was determined at the Th1 and Th2 levels. Airway obstruction was evaluated from endoscopic findings and classified into 3 grades (Grades 0, 1, and 2). Forty-five patients in the control group who underwent tracheal CT for other conditions were retrospectively selected from the database.
Results: Tracheal morphology was abnormal in 50–60%, which showed a transversely collapsing narrow trachea. Tracheal deformity was severe in MPS II and MPS IV. The mean TSA of the MPS patients was 55.5 ± 29.0 mm^2 at Th1 and 61.4 ± 29.0 mm^2 at Th2, while that of the control group was 90.1 ± 41.9 mm^2 and 87.9 ± 39.3 mm^2, respectively. Respiratory distress was noted in 15 of the 35 patients, among whom 7 patients showed tracheal deformity and 7 patients had laryngeal redundancy. Three patients had no abnormalities of the larynx or trachea, so other factors such as pharyngeal stenosis or lower airway stenosis might have contributed to their respiratory distress.
Conclusion: CT and flexible endoscopy allow quantitative and morphological evaluation of airway narrowing, which is beneficial for airway management in MPS children.

© 2014 Elsevier Inc. All rights reserved.

1. Introduction

Mucopolysaccharidoses (MPSs) are lysosomal storage disorders caused by lysosomal enzyme deficiencies that result in the accumulation of glycosaminoglycans (GAGs) in various organs and tissues. Infiltration of GAGs into the oropharynx, joints, and connective tissues can lead to significant upper airway abnormalities, which increase the risk of anesthesia and can cause respiratory distress [1]. Narrowing of the upper airway occurs due to enlargement of the tongue and adenotonsillar hypertrophy, while MPS patients also develop a short immobile neck, thickening of the supraglottic region, and diffuse thickening of the tracheobronchial tree. In addition, respiratory distress is exacerbated by thoracic cage deformity and tracheobronchial abnormalities due to GAG deposition in the soft tissues [2,3]. It was reported that 25% of children with MPS have anatomical airway abnormalities which lead to difficulty with intubation [4]. In some cases, tracheal narrowing has been attributed to complications of endotracheal intubation or tracheotomy and there have also been many reports of sleep-disordered breathing or difficulty with anesthesia. Respiratory distress due to upper airway obstruction and tracheal stenosis is a severe problem that can result in death.

Thus, evaluation of the airway is of primary importance in children with MPS, especially before general anesthesia. Ingelmo demonstrated that performing MDCT of the airways with 3D reconstruction is useful for preoperative evaluation and planning of airway management in MPS patients [5]. However, this method is time-consuming and requires considerable expertise, so it is not suitable for airway screening at all institutions. On the other hand, flexible endoscopy can provide useful information about upper airway problems and is a safe and effective screening method for both preoperative and postoperative uses [6].

The aim of the present study was to investigate changes of the respiratory tract in children with MPS by helical CT and flexible endoscopy.

* Corresponding author at: Department of Otolaryngology, National Center for Child Health and Development, Okura 2-10-1, Setagaya, Tokyo 1578535, Japan. Fax: +81 3 5494 7909.
E-mail address: morimoto-n@ncchd.go.jp (N. Morimoto).

http://dx.doi.org/10.1016/j.ymgme.2014.03.013
1096-7192/© 2014 Elsevier Inc. All rights reserved.

This study represents the first multidisciplinary assessment of both the trachea and the larynx in children with MPS.

2. Materials and methods

2.1. Patients

Thirty-five MPS patients were enrolled in this study. They were aged 2–16 years (mean age: 9.2 ± 4.4 years), their mean height was 117.4 ± 19.1 cm, and their mean BMI was 19.4 ± 3.5. They included 5 patients with Hurler syndrome (MPS I), 25 patients with Hunter syndrome (MPS II), 2 patients with Sanfilippo syndrome (MPS III), 2 patients with Morquio syndrome (MPS IV), and 1 patient with Maroteaux–Lamy syndrome (MPS VI). Patients with prior tracheotomy or congenital thoracic anomalies were excluded. All of the children with MPS I, II, and IV were evaluated prior to initiation of enzyme replacement therapy or BMT.

Forty-five of the control group were retrospectively selected from a database of patients who underwent upper and lower airway CTs for possible pulmonary metastases or other conditions, and they were matched for age (mean age: 8.2 ± 4.5 years; range: 2–15 years) and stature (mean height: 124.0 ± 26.4 cm). Endoscopic evaluation and sleep studies were not performed in the control subjects.

2.2. Tracheal CT

Helical CT was performed by using a high speed CT scanner without contrast enhancement (GE, Discovery 750HD) for both groups. Contiguous 5-mm slices were obtained with the subject in the supine position. Images were obtained during breath holding in expiration as far as possible. The duration of image acquisition from neck to chest was 3 s, which meant that a stable respiratory phase could be maintained.

Tracheal morphology was evaluated at the Th1 and Th2 levels, and was classified into the following 4 categories [7,8]: D-shaped (the transverse diameter is larger than the anteroposterior diameter due to collapse in the latter direction), W-shaped (an elliptical trachea with a larger anteroposterior diameter than transverse diameter due to transverse collapse), O-shaped (slight deformity with a small posterior membranous region), and normal (C-shaped with equal transverse and anteroposterior diameters) (Fig. 1). Single images obtained at the Th1 level and Th2 level were approximated with the mediastinal window in both MPS patients and controls [2], and then the selected images were digitized. Each image was traced twice using an Advantage workstation (GE, Tokyo), and the tracheal cross-sectional surface area (TSA) was calculated at the Th1 and Th2 levels.

2.3. Endoscopic evaluation

The MPS patients underwent endoscopic examination (Pentax, Tokyo, Japan) during spontaneous ventilation and images were captured with a video monitor. The airway was assessed at the level of the epiglottis, the cricoid, and the subglottic region, and findings were graded as follows (Table 1). Grade 0 was a normal airway. Grade 1 meant edema and swelling of the epiglottis or cricoid without redundant mucosa. The false vocal cords showed edema and hypertrophy, partly obscuring the true vocal cords. Grade 2 meant that the redundant mucosa of the epiglottis and cricoid caused inspiratory obstruction, while the true vocal cords were obscured due to hypertrophy of the false cords.

2.3.1. Sleep study

All MPS patients underwent overnight pulse oximetry as a screening test and polysomnography (PSG) was performed as part of the preoperative workup in some patients. Obstructive sleep apnea (OSAS) was

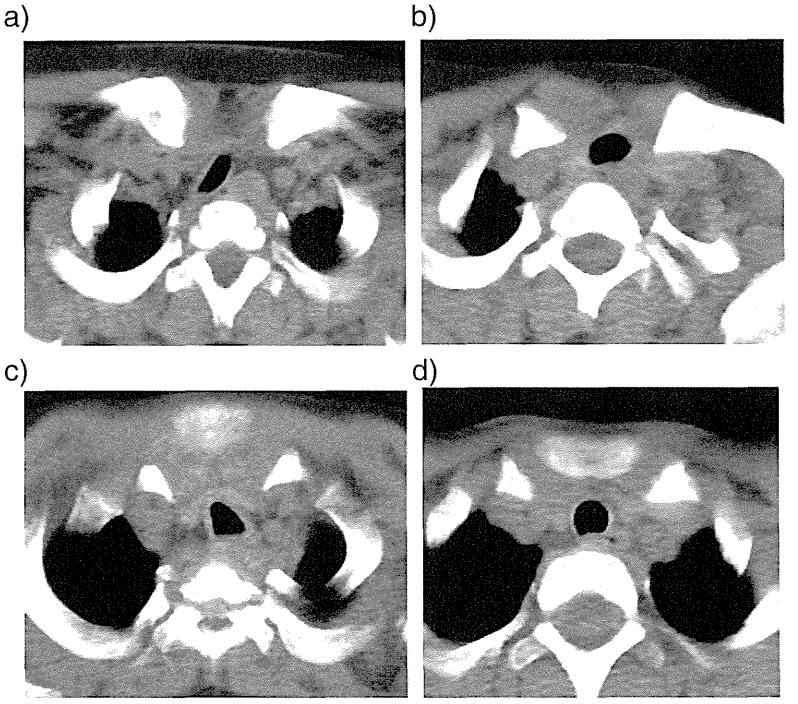

Fig. 1. Morphological change at Th2 level of the trachea. a) W type shows transverse collapse. b) D type shows antero-posterior collapse. c) O type shows deformed trachea slightly. d) Normal trachea.

Table 1
Endoscopic classification of the larynx.

Grade 0	Normal laryngeal structure	
Grade 1	Mucosa is edematous and hypertrophic, but vocal cords are clearly visible.	
Grade 2	Mucosa is edematous and redundant flaccid mucosa cause inspiratory obstruction. Vocal cords are clearly invisible.	

defined as an oxygen desaturation index (ODI) ≥4, which meant that the SpO_2 was at least 4 points lower than baseline ≥4 times per hour.

3. Results

3.1. Morphological analysis of the trachea

Assessment of morphological changes of the tracheal lumen at the Th1 and Th2 levels revealed abnormal morphology at the Th1 level in 17 of the 35 MPS patients (50%), with 2 (6%), 13 (37%), and 2 (6%) patients having a D-shaped, O-shaped, and W-shaped deformity, respectively. When the tracheal lumen was assessed at the Th2 level, morphological abnormality was found in 21 of the 35 patients (60%), with 6 (17%), 7 (20%), and 8 (23%) patients having a D-shaped, O-shaped, and W-shaped deformity, respectively. The characteristics of the tracheal lumen in each type of MPS are shown in Fig. 2. A W-shaped or D-shaped deformity was seen in 11/25 patients with MPS II and 2/2 patients with MPS IV.

3.2. Cross-sectional area of the trachea

In the MPS patients, the mean TSA was 55.5 ± 29.0 mm^2 and 61.4 ± 29.0 mm^2 at the Th1 and Th2 levels, respectively, while the control group had a mean TSA of 90.1 ± 41.9 mm^2 ($p < 0.01$, Student's t-test) and 87.9 ± 39.3 mm^2 ($p < 0.05$, Student's t-test), respectively. The mean TSA of the patients and the control subjects is compared in Fig. 3.

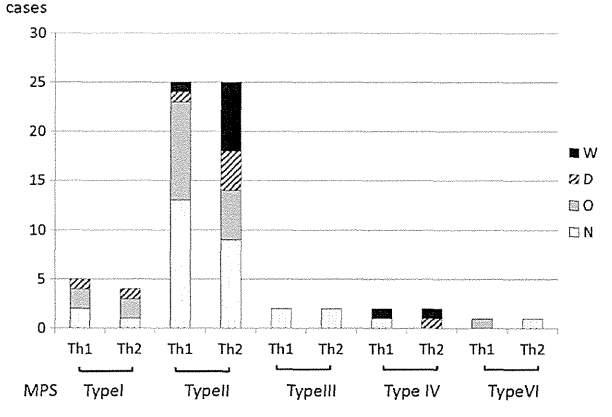

Fig. 2. Tracheal ring deformity at Th1 and Th2 levels. Severe tracheal stenosis was found in Type II and Type IV.

3.3. Endoscopic findings

Endoscopic examination revealed deformity of the laryngeal architecture due to GAG deposition in 23 of the 35 MPS patients (66%). Grade 2 deformity of the arytenoid mucosa was found in 9 of the 35 patients (26%) (Fig. 4a). They had inspiratory stridor and occasional feeding problems associated with coughing and regurgitation, while 5 of them also had sleep apnea. Grade 2 deformity of the false vocal cords caused narrowing of the tracheal airway in 9 patients (Fig. 4b). Grade 2 deformity of the epiglottis was only seen in 2 patients, and was associated with prolapse into the laryngeal inlet.

The clinical respiratory features of the subjects are summarized in Table 2.

3.4. Respiratory features versus anatomical changes

Dysphagia was present in 5 of the 35 patients and required a gastric feeding tube. Four of these 5 patients had MPS II and one had MPS III. All 5 patients showed arytenoid distraction and 3 had a W-shaped trachea. Thirteen of 35 patients had previously undergone adenotonsillectomy because of nasopharyngeal obstruction.

Overnight pulse oximetry showed obstructive sleep apnea (OSA) with a ODI4 > 4 in 15 of the 35 patients, including 2 patients, 12 patients, and 1 patient with MPS I, MPS II, and MPS IV, respectively. Among the 15 patients with OSA, deformation of the arytenoid mucosa and false vocal cords was seen in 10 and 5 patients, respectively. Tracheal deformity was found in 7 of the 15 patients, who had a W-shaped or D-shaped trachea. On the other hand, three of the 15 patients with OSA did not show any abnormalities of the larynx and trachea. Four of the 15 patients with OSA were overweight and had a BMI > 20. In addition, six patients gradually developed upper airway obstruction even after adenotonsillectomy. Three of these six patients had Grade 2 arytenoid deformity and 2 showed tracheal narrowing, but one patient had no abnormalities of the larynx or trachea and the BMI was below 20.

4. Discussion

In patients with mucopolysaccharidoses (MPSs), respiratory problems occur due to upper and lower airway abnormalities. Accumulation of GAGs causes distension of the tongue and pharyngeal mucosa resulting in narrowing of the pharyngeal space [9,1,10,11]. GAG deposition also leads to redundant tissue around the larynx, which prolapses into the respiratory tract. Tracheal stenosis is due to GAG deposition in the tracheobronchial cartilages, which may lead to tracheomalacia [3,2] and can influence both morbidity and mortality [12]. Upper airway obstruction is exacerbated by neck flexion [13], while extension of the neck increases airway patency in MPS IV. GAG deposits cause alveolar and interstitial pulmonary involvement, impairing pulmonary function [14].

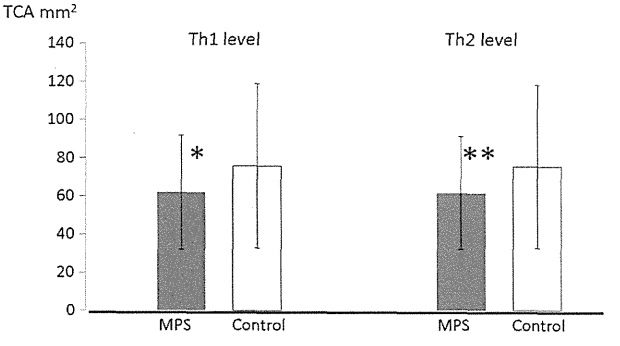

Fig. 3. Tracheal cross-sectional surface area (TSA) at Th1 and Th2. (*$p < 0.01$ and **$p < 0.05$, Student t-test.).

author's personal copy

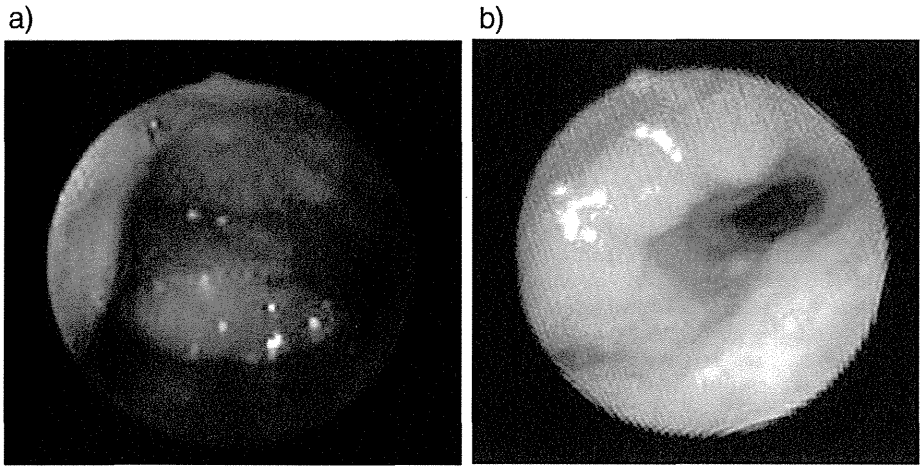

Fig. 4. Endoscopic findings of the larynx. a) Arytenoid deformity as Grade 2. Flaccid arytenoid mucosa is distended to cover the inlet of the larynx. b) Arytenoid deformity (Grade 1) and false vocal cord deformity (Grade 2). Arytenoid mucosa is swelling, hypertrophy of the false vocal cord is thick and glottic space is reduced. Vocal cord is unclear.

Treatment of MPS by enzyme replacement or bone marrow transplantation has significantly altered the natural history of these diseases, but the effects of such therapies on the airway are still unknown [15].

The pathophysiology and prognosis of tracheal stenosis are unclear, because the number of patients with each type of MPS is limited.

4.1. Laryngeal changes

Some authors have tried to classify changes of the larynx into Cormack and Lehane grades by direct laryngoscopy under general anesthesia [16,17], but this is neither easy nor safe because management of

Table 2
Clinical respiratory features of 35 patients in MPS.

				Tracheal lumen		Endoscopic abnormality			Overnight pulse oxymetry	Past history	
	Type	Age (years)	BMI	Th1	Th2	Arytenoid	Epiglottis	Pseudo-vocal	ODI > 4	A/T	Dysphagia
Hurler	I	3	17.2	O	O	1	1	0		+	
	I	6	18.7	N	N	0	0	0		+	
	I	8	17	D	D	0	0	0	+	+	
	I	9	19.5	O	O	0	0	0			
	I	14	16.7	N	N	0	0	0	+	+	
Hunter	II	2	20.5	N	N	2	0	0	+	+	
	II	2	19.7	O	O	2	1	0	+	+	
	II	2	17.8	N	O	1	1	0	+		
	II	3	27.9	N	O	1	0	2	+		
	II	3	19.2	N	N	2	0	0			+
	II	5	20.2	O	N	0	1	0			
	II	5	20.9	N	D	2	0	0			
	II	7	18.9	O	D	2	1	1	+		
	II	7	16.9	N	N	0	0	0		+	
	II	8	19.8	N	N	0	0	0			
	II	8	18.5	N	D	0	0	0	+	+	
	II	8	177	O	W	2	1	2	+	+	+
	II	9	20.1	O	W	0	0	0		+	
	II	11	20.4	N	N	1	0	0	+		
	II	11	23.1	O	O	0	0	0			
	II	11	18.7	N	N	0	0	0	+		
	II	12	16	O	W	2	0	0		+	
	II	13	18.9	N	D	1	1	0			
	II	13	31	N	N	0	0	0	+		
	II	14	19.1	N	W	0	1	2			
	II	14	19.1	O	W	1	1	0	+		
	II	14	18.1	D	W	1	0	0			+
	II	14	19.4	O	N	1	1	0			
	II	16	17	W	W	1	1	2	+		+
	II	16	18.5	0	0	1	2	2		+	
Sanfilippo	IIIA	10	13.4	N	N	2	2	2		+	+
	IIIB	14	15.3	N	N	0	0	0			
Morquio	IV	11	28.6	N	D	1	1	2			
	IV	14	20.5	W	W	2	1	2	+		
Maroteaux–Lamy	VI	6	16	O	N	1	1	2			

Morphological changes of the trachea are classified into 4 types: N; normal, 0; 0 type with a slightly deformed trachea, D; D type with an anteroposterior collapsed trachea, and W; W type with an elliptical shaped stenotic trachea. Endoscopic findings are graded as 0 to 2. 0; normal, 1; mild edematous mucosa, and 2; distended and flaccid mucosa. Overnight pulse oxymetry test shows ODI4 > 4 as an obstructive sleep apnea. A/T: adenotonsillectomy.

general anesthesia itself is difficult due to the respiratory problems of MPS patients.

Deposition of GAGs leads to airway narrowing and redundant tissue which leads to obstruction. In this study, 5 patients had dysphagia that was thought to be caused by arytenoid hypertrophy. The arytenoid mucosa was expanded and flaccid, so that it prolapsed into the laryngeal inlet causing stridor and sometimes dysphagia. Hypertrophy of the false vocal cords reduces the glottic space and was one of the reasons for obstructive sleep apnea in MPS patients, but was not related to dysphagia. Only 2 patients had a flaccid and prolapsing epiglottis, but neither suffered from respiratory distress. Therefore, deformation of the arytenoid mucosa and glottic stenosis seem to be related to respiratory problems in MPS patients. The mucosal changes of the larynx varied with the type of MPS, since severely redundant and flaccid mucosa were noted in MPS II and IV, while abnormal findings were less common in MPS I.

4.2. Tracheal deformity

Half of the MPS children in the present series had abnormal tracheal rings that led to the collapse in the transverse direction (W-shaped deformity) or anteroposterior direction (O-shaped and D-shaped deformity) direction [8]. Shih reported that 8 out of 13 patients (60%) had tracheal deformity [2]. In our series, 17 of 35 patients (49%) had tracheal deformity, so there is a high rate of tracheal morphological changes in MPS patients.

4.3. Airway management

In general, adenotonsillectomy is the first choice treatment for obstructive sleep apnea in children. However, some children with MPS had persistent respiratory distress after surgery in our series due to tracheal stenosis and laryngeal deformity. Because upper airway surgery for MPS children can precipitate respiratory obstruction before or after anesthesia that is occasionally fatal, performance of such surgery should be considered carefully [1].

Tracheal stenosis is one of the major risk factors for intubation and respiratory management under general anesthesia [18,19]. In this study, the cross-sectional tracheal surface area was smaller in MPS children than that in healthy controls, suggesting that anesthesiologists should select a smaller tube than usual for the patient's age [17], and that intraoperative airway management could be difficult for even expert anesthesiologists. A plain X-ray film can suggest the existence of W-shaped tracheal stenosis due to the narrowing of the transverse diameter of the trachea. However, D-shaped tracheal stenosis is more difficult to detect because the transverse diameter is almost normal. If the anteroposterior and transverse diameters of the trachea could be measured prior to endotracheal intubation, tracheal injury might be reduced and perioperative problems could possibly be predicted. Laxity of the laryngeal mucosa is another problem for airway management. Tracheal collapse can occur due to decreased lung volume [20], while a narrow laryngeal inlet, abnormal collapsibility of the trachea, and decreased lung volume cause difficulty with ventilation [21].

4.4. Study limitation

We found that evaluating deformities of the larynx and trachea in MPS children by both CT and flexible endoscopy can be useful for airway management, but this study had several limitations. First, the number of patients was small, so conclusions can be drawn regarding the severity and characteristics of airway changes in each type of MPS. Second, we did not perform pulmonary function tests and we did not assess other factors that could contribute to upper and lower airway obstructions such as nasopharyngeal stenosis, lower airway stenosis, or lingual hypertrophy [11], as well as the influence of thoracic deformity. In this study, no abnormalities of the larynx and trachea were detected in 3 of the 15 MPS patients with sleep apnea, suggesting that other factors also contribute to respiratory problems. Further investigations will be required to clarify such factors. Finally, CT provides useful information for evaluating tracheal deformity, but does not provide data about tracheomalacia or tracheal wall compliance [22]. The scanning time is short for helical CT scan and it is a useful screening method for tracheal abnormality, but it does not provide a dynamic assessment of collapsibility. However, it is clear that many MPS patients have tracheal deformities that vary with the phase of respiration and cause increasing respiratory distress.

Tracheal stenosis can influence mortality in MPS, so the effects of enzyme therapy, bone marrow transplantation, and gene therapy on tracheal changes could be the key to a better prognosis. In this study, all MPS patients were evaluated prior to receiving treatments like enzyme replacement or bone marrow transplantation, which meant that we could not assess the influence of the treatment on airway morphology [19]. Quantitative assessment of tracheal stenosis in MPS using CT and endoscopy might be useful for evaluating the effects of each treatment. Further studies of airway stenosis in children with MPS will be required to provide more information about its influence on the clinical course and about the efficacy of therapy.

Conflict of interest

No conflicts of interested declared.

Acknowledgment

The authors wish to thank Dr. Akari Kimura for the special support with data collection.

Ethics

This study was retrospectively designed and approved by the National Center for Child Health and Development Ethics Committee.

References

[1] M.A. Simmons, I.A. Bruce, S. Penney, E. Wraith, M.P. Rothera, Otorhinolaryngological manifestations of the mucopolysaccharidoses, Int. J. Pediatr. Otorhinolaryngol. 69 (2005) 589–595.
[2] S.L. Shih, Y.J. Lee, S.P. Lin, C.Y. Sheu, J.G. Blickman, Airway changes in children with mucopolysaccharidoses, Acta Radiol. 43 (2002) 40–43.
[3] R. Nagano, S. Takizawa, N. Hayama, S. Umemura, T. Uesugi, S. Nakagawa, S. Okamoto, N. Yanagimachi, S. Takagi, Three-dimensional CT and histopathological findings of airway malacia in Hunter syndrome, Tokai J. Exp. Clin. Med. 32 (2007) 59–61.
[4] R. Walker, K.G. Belani, E.A. Braunlin, I.A. Bruce, H. Hack, P.R. Harmatz, S. Jones, R. Rowe, G.A. Solanki, B. Valdemarsson, Anaesthesia and airway management in mucopolysaccharidosis, J. Inherit. Metab. Dis. 36 (2013) 211–219.
[5] P.M. Ingelmo, R. Parini, M. Grimaldi, F. Mauri, M. Romagnoli, G. Tagliabue, M. Somaini, E. Sahillioglu, G. Frawley, Multidetector computed tomography (MDCT) for preoperative airway assessment in children with mucopolysaccharidoses, Minerva Anestesiol. 77 (2011) 774–780.
[6] M.S. Muhlebach, W. Wooten, J. Muenzer, Respiratory manifestations in mucopolysaccharidoses, Paediatr. Respir. Rev. 12 (2011) 133–138.
[7] C.F. MacKenzie, T.C. McAslan, B. Shin, D. Schellinger, M. Helrich, The shape of the human adult trachea, Anesthesiology 49 (1978) 48–50.
[8] N.T. Griscom, M.E. Wohl, Tracheal size and shape: effects of change in intraluminal pressure, Radiology 149 (1983) 27–30.
[9] C.M. Myer III, Airway obstruction in Hurler's syndrome—radiographic features, Int. J. Pediatr. Otorhinolaryngol. 22 (1991) 91–96.
[10] R.W. Walker, M. Darowski, P. Morris, J.E. Wraith, Anaesthesia and mucopolysaccharidoses. A review of airway problems in children, Anaesthesia 49 (1994) 1078–1084.
[11] F. Santamaria, M.V. Andreucci, G. Parenti, M. Polverino, D. Viggiano, S. Montella, A. Cesaro, R. Ciccarelli, B. Capaldo, G. Andria, Upper airway obstructive disease in mucopolysaccharidoses: polysomnography, computed tomography and nasal endoscopy findings, J. Inherit. Metab. Dis. 30 (2007) 743–749.
[12] H. Steven Sims, J.J. Kempiners, Special airway concerns in patients with mucopolysaccharidoses, Respir. Med. 101 (2007) 1779–1782.
[13] P.P. Walker, E. Rose, J.G. Williams, Upper airways abnormalities and tracheal problems in Morquio's disease, Thorax 58 (2003) 458–459.
[14] G.L. Semenza, R.E. Pyeritz, Respiratory complications of mucopolysaccharide storage disorders, Medicine (Baltimore) 67 (1988) 209–219.
[15] J. Muenzer, Overview of the mucopolysaccharidoses, Rheumatology (Oxford) 50 (Suppl. 5) (2011) v4–v12.

[16] L.K. Koh, C.E. Kong, P.C. Ip-Yam, The modified Cormack–Lehane score for the grading of direct laryngoscopy: evaluation in the Asian population, Anaesth. Intensive Care 30 (2002) 48–51.
[17] K. Kirkpatrick, J. Ellwood, R.W. Walker, Mucopolysaccharidosis type I (Hurler syndrome) and anesthesia: the impact of bone marrow transplantation, enzyme replacement therapy, and fiberoptic intubation on airway management, Paediatr. Anaesth. 22 (2012) 745–751.
[18] S.Y. Shinhar, H. Zablocki, D.N. Madgy, Airway management in mucopolysaccharide storage disorders, Arch. Otolaryngol. Head Neck Surg. 130 (2004) 233–237.
[19] A.H. Yeung, M.J. Cowan, B. Horn, K.W. Rosbe, Airway management in children with mucopolysaccharidoses, Arch. Otolaryngol. Head Neck Surg. 135 (2009) 73–79.
[20] R.C. Heinzer, M.L. Stanchina, A. Malhotra, R.B. Fogel, S.R. Patel, A.S. Jordan, K. Schory, D.P. White, Lung volume and continuous positive airway pressure requirements in obstructive sleep apnea, Am. J. Respir. Crit. Care Med. 172 (2005) 114–117.
[21] M.R. Pritzker, R.A. King, R.S. Kronenberg, Upper airway obstruction during head flexion in Morquio's disease, Am. J. Med. 69 (1980) 467–470.
[22] J.M. Morehead, D.S. Parsons, Tracheobronchomalacia in Hunter's syndrome, Int. J. Pediatr. Otorhinolaryngol. 26 (1993) 255–261